Enhancing the biocorrosion resistance and biocompatibility of Aluminium substrates using Graphene Oxide-PEDOT:PSS Hybrid Coating

*Sourya Subhra Nasker[1], Ragnhild Elizabeth Aune[2], Amogh K. Ravi[3], Tharangattu N. Narayanan[3], and Sasmita Nayak[1,4]**

[1]School of Biotechnology, Kalinga Institute of Industrial Technology (KIIT), Bhubaneswar, Odisha 751024, India
[2]Department of Materials Science and Engineering, Norwegian University of Science and Technology (NTNU), 7491 Trondheim, Norway
[3]Materials and Interface Engineering Laboratory, Tata Institute of Fundamental Research (TIFR), Hyderabad, Telangana 500046, India
[4]Department of Microbiology, Kalinga Institute of Medical Sciences, Kalinga Institute of Industrial Technology Deemed to be University, Bhubaneswar, Odisha 751024, India

**Address all correspondence to Dr. Sasmita Nayak; E-mail: sasmita.n@kiitbiotech.ac.in*

Abstract

In the quest for advanced materials that can effectively combat biofilm-associated infections while ensuring material integrity, graphene oxide coated-aluminum (Al_GO) substrates have emerged as an innovative solution. Despite the well-documented antimicrobial capabilities of graphene oxide, its application at lower concentrations to preserve the structural and biological compatibility of metal alloys remains inadequately explored. This research addresses this gap by optimizing GO coatings at lower concentrations to achieve a balance between antimicrobial efficacy and material biocompatibility. We explored the synergistic combination of electrochemically deposited GO at various concentrations (50, 100, 250, and 500 µg/mL) with PEDOT:PSS on Al (Al_GO/P). This approach aims to create a robust coating that enhances corrosion resistance, biocompatibility, and the antifouling properties of Al, towards biofilm-forming organisms such as *C. albicans*, *S. aureus*, and *E. coli*. Current study identifies that concentrations, particularly 100 and 250 µg/mL of GO on Al exhibit potent biocidal activity, while preserving aforementioned material properties. Since Al is an infinitely recyclable, green material, this work offers a sustainable alternative to traditional antimicrobial surfaces. Further, this presents a strategy for surface modification of implantable biomedical devices, reducing

periprosthetic infection and extending device longevity; as well as for *ex vivo* applications requiring strong antimicrobial performance.

Keywords: *Microbiologically Influenced Corrosion (MIC); Antifouling properties; GO-PEDOT:PSS Coatings; Aluminium Alloy 1050; Biocompatibility.*

1. Introduction

Biofilms, structured microbial communities embedded within a self-produced extracellular matrix (ECM), pose a persistent clinical challenge due to their resilience to conventional therapies and impact on human health[1]. The ECM, also referred to as extracellular polymeric substances (EPS), not only supports nutrient absorption but also enhances microbial defense mechanisms against both host immune system responses and antimicrobial drugs[2]. Biofilm formation on medical devices such as implants, catheters, and ventilators often leads to chronic infections, which reduce the therapeutic effectiveness of interventions against medical device-associated infections (MDAIs). These infections significantly contribute to healthcare-associated infections (HAIs), a critical public health concern that affects approximately one in 31 hospitalized patients each day[3]. HAIs extend hospitalization periods, increase healthcare costs and are predominantly linked to invasive medical devices[3,4]. According to the European Center for Disease Prevention and Control (ECDC), the European Union and European Economic Area (EU/EEA) report over 4.3 million HAI cases annually, resulting in more than 90,000 deaths, exceeding the mortality burden of both influenza and tuberculosis in the region[5–7]. HAIs are also prevalent in the United States, where multidrug-resistant (MDR) infections contribute substantially to high morbidity and mortality rates[8–10]. In India, the burden is particularly severe, with HAI incidence ranging between 11% and 83% depending on the infection type, underscoring systemic vulnerabilities in the healthcare infrastructure[11–15].

Previous research demonstrates that MDAI are typically caused by biofilms comprising mixed microbial communities, including Gram-negative bacteria (e.g., *Escherichia coli* and *Pseudomonas aeruginosa)*, Gram-positive bacteria (e.g., *Staphylococcus aureus*, *Staphylococcus epidermidis*, and *Enterococcus faecalis*), and fungi, predominantly the *Candida* species[16–18]. Microbial adhesion leads to biofouling, which subsequently initiates biocorrosion through the formation of differential aeration cells. These cells accelerate electrochemical degradation and pitting corrosion[19]. Unlike uniform corrosion, pitting results in severe, localized damage that compromises structural integrity and releases cytotoxic metal ions into the surrounding tissues[20]. The complex interplay between biofouling and biocorrosion highlights a key limitation of current implant materials, emphasizing the urgent need for surfaces engineered to resist both microbial colonization and corrosion-induced degradation[21,22].

These challenges reflect broader limitations to traditional implant materials, including stainless steel, aluminum, and synthetic polymers[23]. Their clinical use is often limited by cytotoxic effects, inflammatory host responses, and rapid degradation through either chemical or microbiologically influenced corrosion (MIC), often worsened by biofilm activity[24,25]. Metals and alloys such as 316L stainless steel, cobalt-chromium alloys, and titanium-based materials suffer from long-term performance issues arising from limited biocompatibility and corrosion-induced failure[26]. In chloride-rich physiological environments, mechanical wear and corrosion can release harmful ions such as cobalt, nickel, aluminum, and vanadium, raising significant concerns over systemic toxicity and neurotoxic effects[27,28]. Therefore, there is a clear need for advanced surface engineering strategies to develop materials that effectively mitigate biocorrosion and cytotoxicity without compromising performance[29].

Aluminum alloy AA1050 is widely used in multiple sectors due to its excellent thermal and electrical conductivity[30,31]. As a commercially pure alloy with a minimum aluminum content

of 99.5%, AA1050 is particularly attractive for various applications including packaging, transportation, and electronics[32]. Its relatively lower density further enhances its suitability for aerospace and automotive components[30]. Although AA1050 demonstrates intrinsic corrosion resistance via the formation of a passive oxide layer under dry conditions, this protective barrier becomes compromised in humid or chloride-rich environments[33]. Under such conditions, AA1050 is vulnerable to MIC, as biofilms significantly alter the electrochemical landscape and promote corrosion [34].

To address these issues, recent advances in nanomaterials have facilitated the development of hybrid coatings that limit microbial adhesion and reduce the infection rates associated with devices[35]. Among these, the graphene family of materials (Gfam), especially graphene oxide (GO), has gained attention due to its high surface area, excellent barrier properties, strong adhesion to metals, and broad-spectrum antimicrobial properties[36–40]. When applied to AA1050 at a concentration of 1 mg/mL, GO forms a compact, impermeable barrier that effectively prevents the penetration of corrosive agents such as water, oxygen, and ions[41–44]. Moreover, the integration of the conductive polymer PEDOT:PSS with GO offers a synergistic advantage: GO-PEDOT:PSS hybrid coatings exhibit improved electrical conductivity[45], enhanced conductive pathways[46], and superior electron mobility[47]. Additionally, Singh *et. al.*[48] demonstrated that a GO-PIHA composite coating on copper significantly enhanced corrosion resistance[48].

Given the promising characteristics of the aluminum–graphene oxide-PEDOT:PSS (Al_GO/P) system, several key research questions arise: (1) How does the concentration of GO influence the antifouling efficacy of aluminum substrates against bacterial and fungal pathogens? (2) What GO concentration range provides the optimal balance between antibiofilm activity and biocompatibility? (3) Does the aluminum GO/P system reduce biocorrosion relative to uncoated aluminum under simulated physiological conditions? Addressing these questions is

essential for advancing healthcare-related applications through the strategic optimization of GO-PEDOT:PSS hybrid coatings on AA1050 substrates. Previous work from our laboratory demonstrated that GO coating concentrations in the range of 0.5–1.0 g/L exhibited strong antimicrobial activity but with limited biocompatibility[44]. Therefore, in this work, we evaluated the effect of lower concentrations of GO to achieve an optimal balance between antimicrobial efficacy and biocompatibility. Additionally, we incorporated a conductive polymer PEDOT:PSS at lower concentration (1 µg/mL) to enhance GO adhesion and reduce leaching while preserving the conductivity of the hybrid system. This approach was chosen to synergistically improve antimicrobial performance while minimizing cytotoxic effects.

In the present study, the antifouling performance, biocompatibility, and corrosion resistance of electrochemically deposited PEDOT:PSS polymer (1 µg/mL) integrated with GO at varying concentrations of 50, 100, 250, and 500 µg/mL on aluminum substrates, designated Al_GO50P, Al_GO100P, Al_GO250P, and Al_GO500P, have been evaluated. The modified surfaces were characterized using field emission scanning electron microscopy (FESEM) for GO deposition, Raman spectrophotometry for structural verification, four-point probe measurements for conductivity analysis, and assessments of surface hydrophobicity, adhesion strength, and porosity. The test pathogens, i.e., *Escherichia coli*, *Staphylococcus aureus*, and *Candida albicans*, were selected based on their clinical relevance to HAIs. Antibiofilm activity was assessed via fluorescence microscopy and crystal violet staining, focusing on polymicrobial *Candida*-bacterial biofilms. Mechanistic evaluations included the detection of intercellular reactive oxygen species (ROS) using fluorescent probes and analysis of microbial membrane disruption via SEM analysis. Corrosion rates were measured under both abiotic and biotic conditions according to ASTM standards[49]. Biocompatibility was confirmed through MTT assays, supporting the potential use of these coatings in implantable medical devices, water purification systems, and industrial applications where biofilm mitigation is essential. The

engineered Al_GO/P system thus represents a promising material alternative for improving both device longevity and patient outcomes across sectors.

2. Experimental Procedures

2.1. Substrates synthesis and characterization

2.1.1. Substrate preparation[44,48]

Aluminium plates (AA1050) with 99.5% purity and a thickness of 1.5 mm were obtained from NALCO India Ltd. The precursor graphene oxide (GO, 0.4 wt%) was purchased from Graphenea Inc., and poly(3,4-ethylenedioxythiophene): polystyrene sulfonate (PEDOT:PSS) was obtained from Sigma-Aldrich (Cat. no. #655201). For the experimental procedures, aluminum sheets were sectioned into 2.5 cm × 2.5 cm and 1.5 cm x 1.5 cm squares using an electric discharge machine (EDM) wire cutter. The aluminum substrates were then polished using silicon carbide emery papers of grit sizes ranging from P320 to P2000 to improve surface suitability for electrochemical deposition.

Subsequently, the substrates underwent ultrasonic cleaning in acetone [Cat. no. #31566, SRL] to eliminate any remaining polishing residues and were dried at room temperature.

A facile electrochemical deposition (ECD) process, involving optimization of an aqueous electrolyte, was used to coat the sterile aluminium substrate with a GO-PEDOT:PSS hybrid layer (Al_GO/P). The GO slurry was prepared by dispersing GO in 0.1 M sodium sulfate (Na_2SO_4) [Cat. no. #59977, SRL] to form a Na_2SO_4-GO suspension. The mixture was probe-sonicated for 1 hour to ensure uniform dispersion.

GO suspensions of 50 µg/mL, 100 µg/mL, 250 µg/mL, and 500 µg/mL were prepared. The pH of each suspension was adjusted to a neutral value of 7.0 by adding 0.1 M sodium hydroxide (NaOH) [Cat. no. #68151, SRL] dropwise under continuous stirring.

At this stage, prior to deposition, PEDOT:PSS was added to the GO suspension at a concentration of 1 µg/mL (25 µL).

Electrochemical deposition was carried out in a glass beaker using the cleaned aluminum sheet as the working electrode and a pure copper sheet as the counter electrode. A constant positive DC voltage of 30 V was applied using a Keithley 2601B source meter for 90 seconds to achieve a homogenous, uniform deposition.

Before proceeding to biological experiments, all bare and coated substrates were sterilized by autoclaving at 121°C under 15 lb pressure for 15 minutes, followed by ultraviolet light irradiation for 30 minutes to ensure sterility. Finally, all samples were washed twice with phosphate-buffered saline (PBS) and stored under sterile conditions until use.

2.1.2. Surface morphological analyses: Field emission scanning electron microscopy (FESEM)[44]

FESEM analysis was performed to assess the surface morphology and microstructural variations between the bare aluminum and Al_GO/P-coated substrates. Micrographs were obtained using a JSM-7200F Schottky FESEM (JEOL Ltd., TIFR Hyderabad Facility). The samples (2.5 cm × 2.5 cm) were placed in an ultrahigh vacuum chamber (10^{-6} mbar) and irradiated with high-energy electrons at an accelerating voltage of 5 kV.

To enhance surface conductivity and image resolution, samples were sputter-coated with a thin layer of gold prior to imaging. Observations were conducted using the secondary electron (SE) detection mode to obtain high-contrast micrographs of surface features.

2.1.3. Raman Spectrophotometry[50]

The structural identity of the GO layer in the Al_GO/P samples was characterized using a Renishaw inVia™ confocal Raman microscope. The Raman spectra were recorded at 25°C using a 532 nm laser as the excitation source. Spectral data were collected in the range of 101 cm^{-1} to 3202 cm^{-1} with a resolution of 0.8 cm^{-1}.

2.1.4. Water Contact Angle (WCA)[51]

The surface wettability of both bare aluminum and the Al_GO/P substrates was evaluated by measuring the static water contact angle (WCA) using a VCA Optima contact angle meter (AST Products Inc.). The sessile drop technique was employed, in which a droplet of ultrapure water was placed on the surface of each specimen. Images of the droplet were captured and analyzed to determine the contact angle, thereby indicating the relative hydrophobicity or hydrophilicity of the surface. The measurements were repeated at multiple points per sample to ensure reproducibility.

2.1.5. Four-probe conductivity measurement [52]

Bulk electrical conductivity of bare and Al_GO/P substrates was measured using the Van der Pauw method. A four-probe station and Keithley 2450 source meter (delta mode) were used for this purpose. Electrical contacts were placed at the edges of the substrate, and a 10 mA current was applied to measure the sheet resistance (R_s).

The bulk conductivity (σ) was calculated using the relation:

$$\sigma = \frac{1}{R_S t} \qquad \text{(Eq. 1)}$$

where t is the thickness of the aluminum substrate. All measurements were conducted under controlled ambient conditions, and the conductivity values were compared across different GO concentrations.

2.1.6. Porosity Evaluation [44,53–55]

The porosity of the hybrid coating was evaluated using electrochemical techniques in a 3.5 wt.% NaCl solution,[44,53–55] simulating a corrosive environment. A three-electrode setup was configured using a VSP-300 multichannel potentiostat/galvanostat (BioLogic, France). The working electrode was either a bare or coated aluminum substrate, the reference electrode was Ag/AgCl, and the counter electrode was a platinum mesh.

The active surface area was defined using an epoxy mask, exposing only 1 cm^2 of the sample. The open circuit potential (OCP) was monitored for 30 minutes until stabilization. Tafel polarization was carried out at a scan rate of 1 mV/s, over a potential range of ±250 mV relative to OCP at room temperature.

Tafel parameters, i.e., corrosion potential (E_{corr}) and anodic Tafel slope (β_a), were extracted using EC-Lab software.

Electrochemical impedance spectroscopy (EIS) was performed with an AC amplitude of 10 mV over a frequency range of 100 kHz to 100 mHz. Data fitting was carried out using equivalent circuit models to determine the polarization resistances (R_P) of both coated and uncoated samples.

The porosity P (%) was calculated using the following equation[56],

$$P = \left(\frac{R_{PS}}{R_P}\right) \times 10^{-\left(\frac{\Delta E_{corr}}{\beta_a}\right)} \qquad \text{(Eq. 2)}$$

where R_{PS} is the polarization resistance of the coated substrates, R_p the polarization resistance of the bare aluminum substrate, ΔE_{corr} the difference between the corrosion potential of the coated ($E_{corr,coatings}$) and bear ($E_{corr,A}$) substrates ($\Delta E_{corr}=E_{corr,coatings} - E_{corr,Al}$), and β_a the anodic Tafel slope of the bare aluminum.

222 **2.2. Antimicrobial and Antibiofilm Assay**

223 *2.2.1. Microbial cell culture*

224 *Candida albicans* (*C. albicans*) [fungus, ATCC 76485] cells were cultivated on Yeast-Peptone
225 Dextrose (YPD) agar [Cat. no. #G038, HiMedia] plates at 30°C for 24 hours. A single colony
226 was selected and inoculated into YPD broth [Cat. no. #M1363, HiMedia], which was then
227 incubated overnight at 25°C with shaking at 200 rpm. From this overnight culture, a secondary
228 culture was initiated at a 1:100 dilution and allowed to grow until it reached the mid-
229 logarithmic phase. The final fungal cell suspension was prepared to achieve a concentration of
230 10^8 CFU/mL.

231 *Escherichia coli* (*E. coli*) [Gram-negative bacterium, ATCC 29425] and *Staphylococcus aureus*
232 (*S. aureus*) [Gram-positive bacterium, ATCC 25923] cells were grown on Luria Bertani (LB)
233 agar [Cat. no. #G1151, HiMedia] plates at 37°C for 24 hours. A single colony was picked and
234 inoculated into LB broth [Cat. no. #G1245, HiMedia], followed by overnight incubation at
235 37°C with shaking at 200 rpm. From this culture, a secondary inoculum was prepared using a
236 1:100 dilution, which was then grown to the mid-logarithmic phase. The final bacterial cell
237 suspension was prepared to achieve concentrations of 10^7 CFU/mL and 10^8 CFU/mL,
238 depending on the assay.

239 For mixed *Candida*-bacterial biofilms, a suspension was prepared by mixing 1 mL each of the
240 *C. albicans*, *S. aureus*, and *E. coli* cultures in a 1:1:1 ratio [57].

241

242 *2.2.2. Microbial Growth Inhibition Assay*[50,58]

243 The Al_GO/P substrates (2.5 cm × 2.5 cm) were sterilized by autoclaving at 121°C for 15
244 minutes under 15 lb pressure, followed by ultraviolet light exposure for 30 minutes. 100 µL of

245 bacterial suspension containing 10^7 CFU/mL was pipetted onto different Al_GO/P and control
246 substrates (Glass and Bare Al) inside sterile Petri plates. These were incubated at 37°C for 2
247 hours under aseptic conditions.

248 After incubation, molten LB agar (45ºC) was poured over the substrates and allowed to solidify
249 at room temperature. The plates were then incubated overnight at 37°C, and bacterial colonies
250 were analyzed the following day.

251 Similarly, 100 µL of *C. albicans* suspension (10^7 CFU/mL) was incubated on distinct Al_GO/P
252 and control substrates in sterile Petri plates for 10 hours under aseptic conditions. Following
253 incubation, molten YPD agar (45ºC) was poured over the surfaces and allowed to solidify. The
254 plates were incubated overnight at 30°C, and fungal colonies were analyzed after 24 hours.

255 *2.2.3. Antibiofilm assay*[44]

256 A mixed microbial suspension was incubated on sterilized Al_GO/P substrates (150 µL/cm²)
257 placed in sterile Petri dishes at room temperature. To maintain constant humidity, the plates
258 were placed in closed containers containing autoclaved deionized water channels to prevent
259 desiccation stress.

260 The mixed suspension was seeded onto both control and Al_GO/P-coated substrates and
261 incubated for 10 hours. Two different inoculum concentrations (10^7 CFU/mL and 10^8 CFU/mL)
262 were tested in parallel to assess biofilm formation. After incubation, 100 µL of each residual
263 suspension was transferred to 35mm Petri plates containing a 1:1 mixture of YPD and LB
264 broth, supplemented with 10% fetal bovine serum (FBS) [Cat. no. # A5256901, Gibco], and
265 incubated at 37°C for an additional 10 hours.

266

267 *2.2.4. Fluorescence microscopy to visualize biofilm formation*

268 After 10 hours of incubation under biofilm-stimulating conditions (37°C with 10% FBS),
269 biofilm-coated substrates were gently washed with sterile distilled water to remove planktonic
270 cells. The remaining biofilm biomass was sequentially stained using dark conditions with:

271 • Calcofluor white [Cat. no. #18909, Sigma-Aldrich] for *C. albicans* (blue) [59–61]
272 • Acridine orange [Cat. no. #A9231, Sigma-Aldrich] for *S. aureus* (red)[62]
273 • Sodium fluorescein [Cat. no. #46960, Sigma-Aldrich] for *E. coli* (green)[63]

274 The dyes were prepared according to established protocols[63]. Fluorescence imaging was
275 performed using an EVOS Cell Imaging Station (Invitrogen) at 40× magnification.

276 *2.2.5. Biofilm biomass quantification*[64]

277 Following 10-hour incubation, 100 µL of each suspension was seeded into wells of a 96-well
278 plate containing YPD medium supplemented with 10% FBS and incubated at 37°C under static
279 conditions for an additional 10 hours.

280 The biofilms were washed three times with Milli-Q water to remove non-adherent cells. Then,
281 200 µL of 0.1% (w/v) crystal violet solution [Cat. no. #TC510, HiMedia] was added to each
282 well, and the plates were incubated at room temperature for 30 minutes on an orbital shaker at
283 70 rpm.

284 Excess stain was removed with three washes using Milli-Q water, and the wells were dried at
285 room temperature for 30 minutes. The retained stain was solubilized with 200 µL of 70% (v/v)
286 ethanol, and absorbance was measured at 595 nm.

287 • Growth control (GC): Glass substrate (100% biofilm)
288 • Sterility control (SC): Ultrapure water (0% biofilm)

289 Percentage biofilm growth was calculated using the following equation:

290 $$\% \, Biofilm \; growth = \frac{Sample_{A595} - SC_{A595}}{GC_{A595} - SC_{A595}} \; x \; 100 \qquad \text{(Eq.3)}$$

291 where $Sample_{A595}$ is the absorbance of the test substrate, SC_{A595} the absorbance of the sterility
292 control (0% biofilm), and GC_{A595} the absorbance of the growth control (100% biofilm).

293 *2.2.6. Detection of ROS production*[44,65]

294 Mixed *Candida*-bacterial suspension was seeded on sterile Al_GO/P substrates and incubated
295 at room temperature for 10 hours under constant humidity. 10 µM of 2',7'-
296 dichlorodihydroflourescein diacetate (H_2DCF-DA) [Cat. no. #D399, Invitrogen] was added to
297 the suspension and incubated for 20 minutes in the dark. Imaging was performed using an in-
298 house fluorescence microscope (Floid cell station, 40×, Invitrogen).

299 To detect surface-generated ROS, 10 µM of H_2DCF-DA was applied directly onto washed
300 substrates, and green fluorescence was recorded using a Nikon ECLIPSE Ci-E microscope at
301 40× magnification.

302 Mixed bacterial cell suspension was seeded on sterile Al_GO/P substrates and incubated at
303 room temperature for 10 hours under constant humidity. A 10 µM solution of the cytosolic
304 superoxide indicator dye dihydroethidium (DHE) [Cat. no. #D1168, Invitrogen] was used to
305 stain the suspension for 20 minutes in the dark[66]. Following incubation, cell imaging was
306 performed using an in-house fluorescence microscope (Floid Cell Station, 40×, Invitrogen).

307 To detect ROS generated at the material surface, a separate experiment was performed: mixed
308 bacterial cell suspension was seeded on sterile Al_GO/P substrates and incubated at room
309 temperature for 10 hours under constant humidity. After incubation, the substrates were rinsed
310 and placed under a fluorescence microscope. A 10 µM solution of DHE was then applied
311 directly to the surface of both the control and Al_GO/P substrates. The resulting red

312 fluorescence signal was captured using a Nikon ECLIPSE Ci-E microscope at 40×
313 magnification.

314 *2.2.7. Scanning electron microscopy* (*SEM*)[44,50]

315 10^7 CFU of the mixed *Candida*-bacterial suspension were incubated over sterilized Al_GO/P
316 substrates (150 µL/cm^2) placed in sterile Petri plates at room temperature for 10 hours under
317 constant humidity. Following incubation, the cells were fixed with 2.5% glutaraldehyde and
318 dehydrated through a graded ethanol series (30%, 60%, 70%, 80%, 90%), followed by
319 treatment with 100% ethanol for 30 minutes.

320 The substrates were then sputter-coated with gold-palladium and imaged using a Gemini SEM
321 450 (Zeiss, KIIT Central Research Facility).

322 **2.3. Evaluation of Corrosion Resistance**

323 *2.3.1. Description of immersion systems* [34]

324 The experiments were carried out in two systems consisting of glass beakers with a usable
325 volume of 300 mL, in which the substrates were fixed to the bottom after prior sterilization.
326 The medium employed was a 1:1 mixture of LB and YPD broth, sterilized in an autoclave at
327 121°C and 15 lb pressure for 15 minutes. Both systems were assembled under aseptic
328 conditions.

329 The abiotic system (control) contained only the sterile medium along with the following
330 antibiotics: Fluconazole (antifungal, 15 µg/mL) [Cat. no. #22239, SRL], Chloramphenicol
331 (antibacterial, 15 µg/mL) [Cat. no. #97686, SRL], and Vancomycin (antibacterial, 15 µg/mL)
332 [Cat. no. #61078, SRL]. The biotic system included the same sterile medium, supplemented
333 with 1% (v/v) of the mixed *Candida*-bacterial inoculum.

334 *2.3.2. Weight loss measurement of the corroded substrates*

After 45 days of exposure in both biotic and abiotic systems, weight loss was calculated following the chemical cleaning procedure described in ASTM G1-03 standard[49]. After removal of the biofilm, the samples were immersed in a 69.2 wt% nitric acid solution for approximately 5 minutes to remove corrosion products, rinsed with distilled water to eliminate residual acid, and then dried under flowing air.

The specimens were weighed before and after the experiment using an analytical balance, and the corrosion rate was calculated using the following equation:

$$Corrosion\ rate = \frac{(W\ x\ K)}{(A\ x\ T\ x\ D)}\ \mu mpy \qquad \text{(Eq. 4)}$$

where W is the weight loss, K the unit conversion constant (8.76 x10^7), A the exposed area, T the exposer time, D the material density, and μmpy the corrosion rate.

The measured corrosion rates were classified according to the NACE Standard RP-07-75[67], which provides validated guidelines for the preparation, analysis, and interpretation of corrosion measurements. All tests were performed in triplicate.

2.3.3. FESEM analysis of immersed Al_GO/P substrates

FESEM was used to investigate microstructural variations in the bare aluminum and the Al_GO/P substrates before and after 45-day immersion in both abiotic and biotic environments.

To observe the corrosion morphology, the substrates were cleaned in accordance with the ASTM G1-03 standard[49]. Micrographs were obtained using a JSM-7200F Schottky FESEM (JEOL Ltd., TIFR Hyderabad Facility), operated at an accelerating voltage of 30 kV. Samples of 2.5 cm × 2.5 cm were placed in an ultrahigh vacuum chamber (10^{-6} mbar). Prior to imaging, substrates were coated with a thin gold film to enhance surface conductivity and enable high-resolution image capture.

2.4. Cytotoxicity assay

358 *2.4.1. Mammalian Cell Culture* [68–71]

359 The Human Embryonic Kidney (HEK293T) cell line [ATCC CRL-11268] was used. HEK293T
360 is a well-established model and is widely employed in cytotoxicity assays, including the
361 evaluation of new biomaterials[72]. A frozen vial was retrieved from liquid nitrogen storage and
362 thawed using a standard defrosting protocol. The cells were cultured in Dulbecco's Modified
363 Eagle Medium (DMEM) [Cat. no. #10564011, Gibco] supplemented with 10% fetal bovine
364 serum (FBS) [Cat. no. # A5256901, Gibco] and 1X Antibiotic-Antimycotic solution [Cat. no.
365 #A002, HiMedia]).

366 Cells were maintained at 37°C in a humidified incubator with 5% CO_2 and 95% air. Upon
367 reaching approximately 80% confluency, biocompatibility experiments were initiated. Cell
368 counting was performed using a hemocytometer. Samples were prepared according to Sections
369 4.2 and 4.3 of ISO 10993-5: Biological Evaluation of Medical Devices - Part 5: Tests for In
370 Vitro Cytotoxicity, and the experiments were performed in compliance with Section 8 of the
371 same standard[73].

372 *2.4.2. Indirect (extract) assay*

373 HEK293T cells were seeded into 96-well plates at a density of $1x10^4$ cells per well and
374 incubated for 24 h. In parallel, extracts of the test materials were prepared. After sterilization
375 with 70% ethanol and ultraviolet light exposure for 30 minutes, the Al_GO/P substrates were
376 placed in 35 mm Petri plates containing fresh growth medium. The extraction procedure was
377 carried out at 37°C for 24 hours to obtain 100% crude extracts.

378 Once the seeded cells reached approximately 70% confluency, the culture medium was
379 replaced with the test extracts. Cells were incubated for an additional 24 and 48 hours. Each
380 condition was tested in triplicate.

381 Cell viability was assessed by incubating the cells in medium containing 0.5 mg/mL of 3-[4,5-
382 dimethylthiazol-2-yl]-2,5-diphenyltetrazolium bromide (MTT) [Cat. no. #CCK003, HiMedia]
383 for 2 hours. The medium was then replaced with isopropanol to solubilize the purple formazan
384 product, and absorbance was measured at 570 nm. Results are expressed as the percentage of
385 MTT signal relative to untreated control cells, which were defined as 100% viable.
386 Experiments were conducted according to Section 8.2 of ISO 10993-5: Biological Evaluation
387 of Medical Devices - Part 5: Tests for In Vitro Cytotoxicity[73].

388 *2.4.3. Direct contact assay*

389 HEK293T cells were seeded into 35 mm Petri plates and incubated for 24 and 48 hours in the
390 presence of pre-sterilized test samples (70% ethanol and ultraviolet light-treated), which were
391 carefully placed in the center of each plate. Each test material was evaluated in triplicate.

392 After incubation, cell viability was measured directly by adding 0.5 mg/mL MTT reagent to
393 the culture medium and incubating for 2 hours. The medium was then replaced with
394 isopropanol to extract the formazan dye, and absorbance was measured at 570 nm. Results
395 were reported as percentage MTT signal compared to the control, where untreated cells were
396 set at 100% viability. All procedures were carried out in compliance with Section 8.3 of ISO
397 10993-5: Biological Evaluation of Medical Devices - Part 5: Tests for In Vitro Cytotoxicity[73].

398

399

400

401

402

403

3. Results and Discussion

3.1. Material property assessment

3.1.1. Synthesis of Graphene oxide – PEDOT:PSS hybrid coated Aluminium (AA1050) substrates

The schematic diagram illustrating the facile two-step synthesis process for graphene oxide-coated Al substrates is presented in Figure 1. The inherent negative surface charge (zeta potential) of the aqueous GO dispersion causes anodic deposition at applied potentials of 10 volts or higher[44]. These electrostatic forces were sufficient to drive GO nanosheets toward the working electrode – the Al substrate[74]. As aforementioned, previous work from our lab showed that GO coatings at 0.5–1.0 g/L offered strong antimicrobial activity but poor biocompatibility, hence, we employed lower concentrations to balance antimicrobial activity vs biocompatibility[44]. Further, PEDOT:PSS was used at a reduced concentration (1 µg/mL) in the hybrid system to preserve conductivity while enhancing the adhesion of GO to the underneath metal. The sample preparation parameters for coating AA1050 substrates using GO (50, 100, 250, and 500 µg/mL) with PEDOT:PSS (1 µg/mL) is detailed in Table 1.

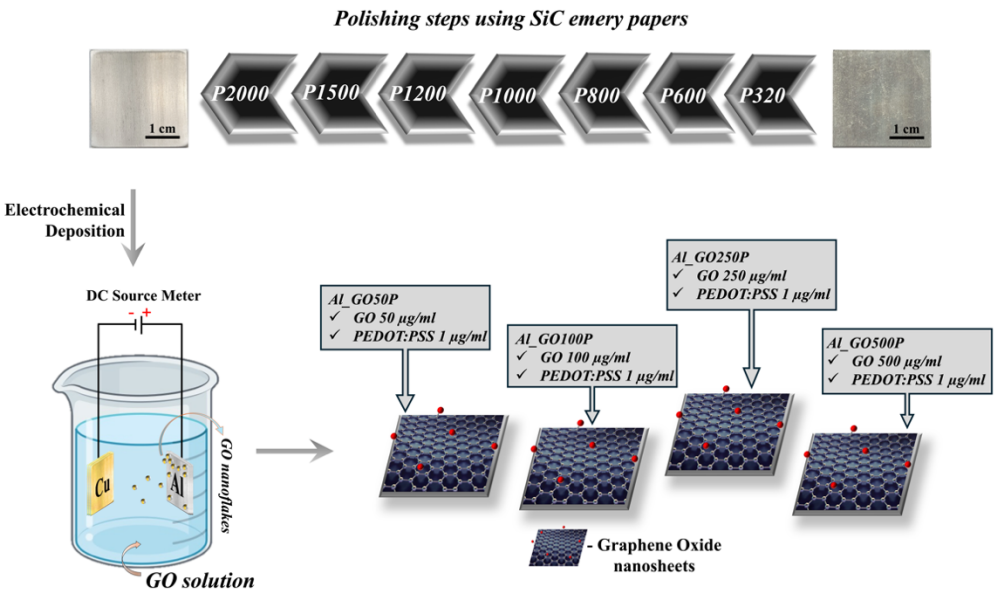

Figure 1. Facile two-step synthesis process of GO coated AA1050 substrates. Schematic diagram illustrating the preparation of Al_GO/P substrates, including sequential polishing of aluminum using SiC papers of varying grit sizes, followed by electrochemical deposition.

Table 1. The details of sample preparation parameters used for coating Al substrates using varied concentration of graphene oxide sourced from Graphenea Inc.

Sample Code	*GO concentration (in µg/mL)*	*PEDOT:PSS concentration (in µg/mL)*	*Voltage applied (in Volts)*	*Duration of deposition (in seconds)*
Al_GO50P	50	1	30	90
Al_GO100P	100	1	30	90
Al_GO250P	250	1	30	90
Al_GO500P	500	1	30	90

3.1.2. Raman Spectrophotometry confirmed identity of GO on Al_GO/P substrates

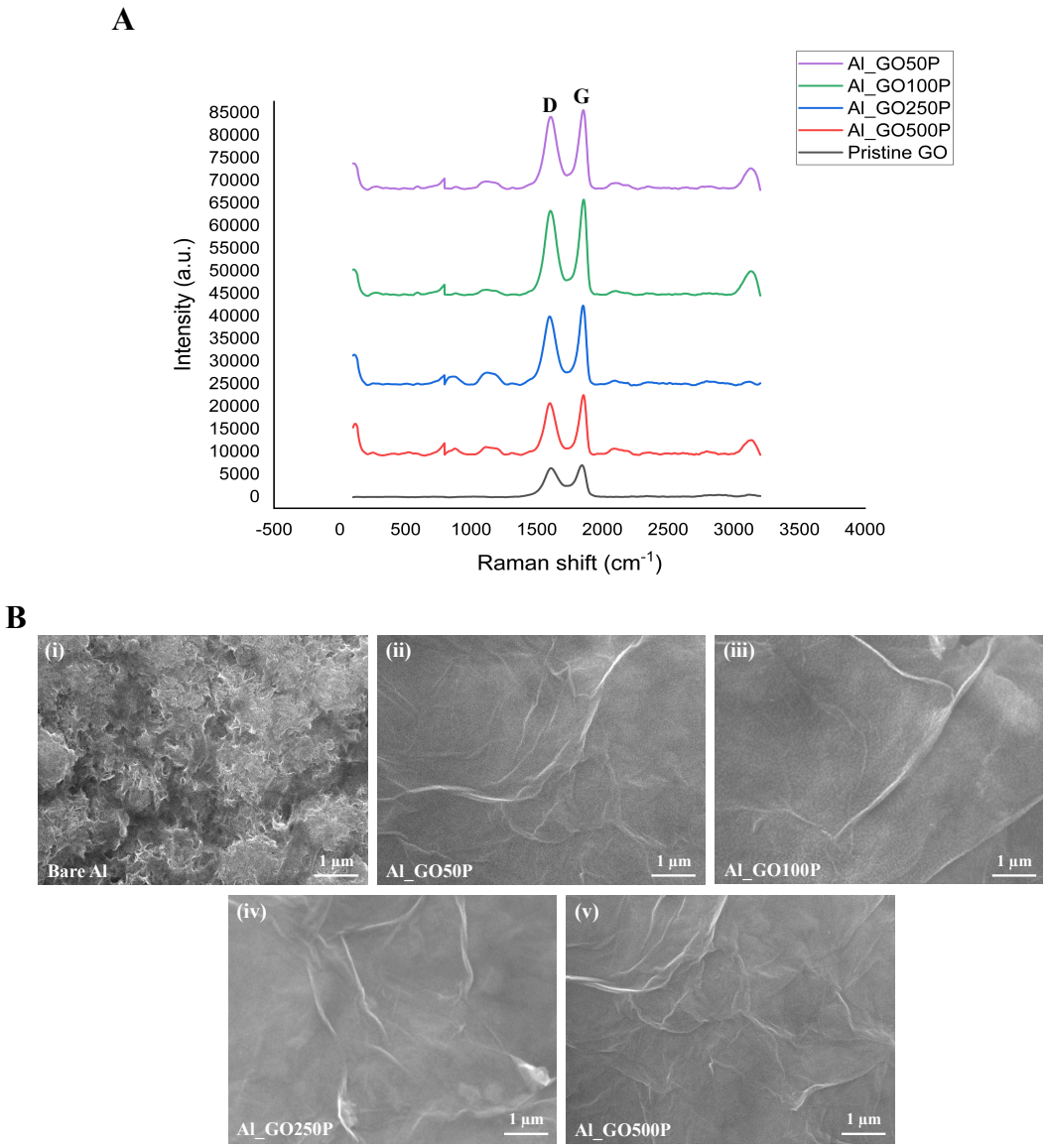

Figure 2. (A) Raman spectra of graphene oxide (GO) and Al_GO/P substrates. The figure shows the Raman signatures (D and G peaks) of GO and the fabricated Al_GO/P substrates at different Y-offset positions. **(B) FESEM micrographs of bare Al vs Al_GO/P surfaces.** FESEM images showcase (i) polished Al, and uniform deposition of GO on Al_GO/P substrates: (ii) Al_GO50P, (iii) Al_GO100P, (iv) Al_GO250P, and (v) Al_GO500P.

Raman spectroscopy serves as a widely employed tool for acquiring structural insights into carbon-based materials. The Raman spectra of graphitic carbon-based materials primarily

manifest the G and D peaks, and their overtones. In Figure 2A, we present the Raman spectra of GO and various Al_GO/P substrates. Notably, the most prominent peaks emerge as the G band, occurring at approximately 1594 cm^{-1}, and the D band, situated around 1328 cm^{-1} as evidenced in prior literature[44,51]. The G peak primarily arises from the bond stretching of sp^2 carbon atom pairs, encompassing both ring and chain structures[75]. In contrast, the D peak is indicative of structural defects within the graphene lattice. Moreover, the variation in intensity ratios of the D and G bands reveal the characteristics of GO deposited on Al_GO/P substrates as shown in Table S1 (Supporting Information). GO exhibited an I_D/I_G ratio of 0.91, which increased slightly to 0.92 for Al_GO50P, then decreased to 0.88 for Al_GO100P, and further to 0.86 for both Al_GO250P and Al_GO500P (Table S1, Supporting Information). These results confirm the successful deposition of GO on the various Al_GO/P surfaces as shown in prior literature[44,76].

Additionally, we verified the identity of commercial PEDOT:PSS via Raman spectroscopy (Figure S1, Supporting Information). The most prominent Raman band, located around 1437 cm^{-1}, consistently exhibits a well-reproducible symmetric profile with a mixed pseudo-Voigt line shape (Figure S1, Supporting Information). Interestingly, this prominent band also displays the most substantial variation, encompassing a total shift of approximately 10 cm^{-1} within the PEDOT:PSS complex. Furthermore, our observations of the Raman signatures for the PEDOT:PSS utilized in this study are in strong concurrence with the Raman spectrum obtained from previous research[77,78]. This agreement underscores the reliability and consistency of the Raman spectroscopic characteristics of the PEDOT:PSS material used in the coating process.

3.1.3. FESEM confirmed uniform deposition of GO on Al surfaces

Electrochemical deposition (ECD) of GO on Al surface is expected to produce a smooth and uniform coating, as the quality of the coating is determined by its homogeneity[48,79]. FESEM

micrographs of the bare Al and Al_GO/P substrates are shown in Figure 2B, providing visual evidence of GO nano-sheets overlaying on the Al substrate The polished Al surface exhibits a non-uniform and rough surface morphology characterized by the presence of potholes and cavities.. However, the FESEM images of Al_GO/P substrates demonstrated smooth GO sheets with small wrinkles and folded at the edges as is evidenced from existing literature[44,50]. FESEM micrographs, therefore, confirmed the uniformity of the GO coatings on Al_GO/P surface.

3.1.4. Hydrophobic and Conductive nature of Al_GO/P surfaces confirmed by water contact angle (WCA) and four-probe conductivity measurements

The deposition of GO on Al substrates has been observed to enhance the surface hydrophobicity[44]. This increase in hydrophobicity is attributed to the uniform GO coating, which alters the surface energy and reduces wettability[80,81]. Consequently, we evaluated the wettability of the bare Al surface and the Al_GO/P substrates, relying on the stationary WCA measurements (Table 2 and Figure S2, Supporting Information). The water contact angle of bare Al was 85.1° but increased to over 90° for all Al_GO/P surfaces, showing an increase in surface hydrophobicity (Table 2 and Figure S2, Supporting Information). Among the samples, Al_GO500P had the highest WCA at 120.2°, followed by Al_GO250P (114.9°), Al_GO100P (106.8°), and Al_GO50P (101.6°).

Additionally, the electrical conductivity measurements for bare Al and Al_GO/P substrates are detailed in Table 2. It is worth noting that pure aluminum possesses inherently high electrical conductivity, registering at 3.43×10^{7} S/m (equivalent to 59.14% of the International Annealed Copper Standard, IACS), consistent with previous literature[82]. The conductivity of the aluminum alloy AA1050 was determined to be 3.11×10^{7} S/m, which is slightly lower than that of pure aluminum but falls within the same order of magnitude. It was observed that while the

conductivity of the Al_GO/P substrates shows a relative reduction compared to the bare Al surface used in this study, the values were within the conductivity ranges for known materials [83–85]. Moreover, this reduction in conductivity becomes more obvious with increasing GO concentration as detailed in Table 2. This phenomenon can be attributed to the inherent insulating nature of graphene oxide, as previously documented[86]. It is plausible that the reduction in conductivity is a consequence of the expansion of interlayer spacing among the GO nanosheets due to the presence of functional groups within the basal planes[87].

Table 2. Stationary water contact angle (WCA) and electrical conductivity values of the synthesized Al_GO/P substrates and control surface, bare Al.

Samples	***WCA (in degrees)***	***Electrical Conductivity* (S/m) x 10^7**
Bare Al	*85.1 ± 0.42*	*3.11 ± 0.67*
Al_GO50P	*101.6 ± 0.95*	*2.17 ± 0.47*
Al_GO100P	*106.8 ± 0.21*	*1.95 ± 0.19*
Al_GO250P	*114.9 ± 4.53*	*1.78± 0.2*
Al_GO500P	*120.2 ± 2.88*	*1.61 ± 0.43*

3.1.5. Porosity evaluation of Al_GO/P substrates

The presence of porosity in coatings directly correlates to lower density and reduced compactness of the coating than the bulk metal[55]. Moreover, a porous coating decreases their protective ability as it allows foreign particles, microorganisms, or corrosive ions to reach and potentially damage the underlying metal, and cause corrosion. The corrosion potential (E_{corr}) and anodic potential (β_a) for pure aluminium and Al_GO/P substrates were determined through Tafel fitting of the linear polarization responses in Figure S3 (Supporting Information) using

EC-Lab software. Polarization resistances were derived from the Nyquist impedance plot (Figure S4, Supporting Information) via Z-Fitting in EC-Lab software.

The details for the porosity measurements for GO coatings is described in the Experimental Section and the results are provided in Table 3. The Al_GO/P substrates exhibited porosities of 60.2% (Al_GO50P), 34.7% (Al_GO100P), 10.9% (Al_GO250P), and 9.5% (Al_GO500P), demonstrating a significant reduction in porosity with increased GO concentration(s) on the Al surface(s). As per prior literature porosity measurements have been correlated to the antimicrobial efficacy of coated materials[44,88].

Table 3. Electrochemical characteristics of bare Al and Al_GO/P substrates and porosity (%) calculation

Sample	Polarization Resistance, R_{PS}	Polarization Resistance, R_P	Corrosion Potential, $E_{corr,Al}$ (V)	Corrosion Potential, $E_{corr,Coatings}$ (V)	Anodic Potential, $\beta_{a,Al}$ (mV)	Porosity (%)
Al_GO50P	1670	2765	-0.73	-0.47	158.3	60.2
Al_GO100P	1670	4788	-0.73	-0.47	158.3	34.7
Al_GO250P	1670	15330	-0.73	-0.48	158.3	10.9
Al_GO500P	1670	17550	-0.73	-0.48	158.3	9.5

3.2. Assessment of antimicrobial potential of Al_GO/P substrates

3.2.1. Al_GO/P inhibited growth of microbial cells

In a preliminary study, growth inhibition assay was conducted to evaluate the antimicrobial activity of the fabricated Al_GO/P substrates. This is a conventional technique where microbial cells are exposed to substrates for a specific time, followed by growth on nutrient rich medium overnight[50]. The antibacterial and antifungal activities of Al_GO/P substrates (Al_GO50P, Al_GO100P, Al_GO250P, and Al_GO500P) were tested against Gram-positive *S. aureus*, Gram-negative *E. coli*, and fungus *C. albicans*. Bare Al (uncoated Al sheet) and glass slides were used as control surfaces.

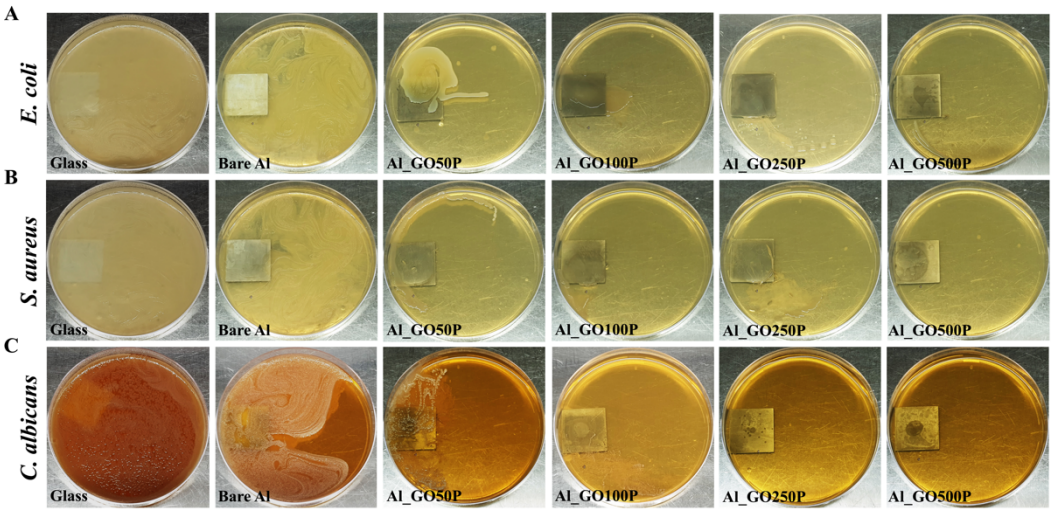

Figure 3. Growth Inhibition Assay of Al_GO/P substrates. After 10 hour of incubation on different control (glass and bare Al) and Al_GO/P substrates, (**A, B**) bacterial (*E. coli, S. aureus*) and (**C**) fungal (*C. albicans*) cells were cultured on LB and YPD agar plates, respectively. The inhibitory roles of the coated substrates were assessed by examining colony growth the following day. Cells cultivated on glass and bare Al surfaces exhibited abundant bacterial and fungal colonies, indicating a lack of antimicrobial potential. In contrast, cells cultured on Al_GO50P presented minimal colony growth while rest of the Al_GO/P substrates demonstrated no visible colony growth.

Figures 3A, 3B and 3C show the bacterial (Gram-positive *S. aureus* and Gram-negative *E. coli*) and fungal (*C. albicans*) colonies on LB and YPD agar plates, respectively. Control surfaces glass and bare Al displayed rich growth of microbial colonies for both bacterial and fungal species. However, significantly low colony growth was observed on Al_GO50P substrate. Further, no bacterial and fungal cell growth were noted on rest of the Al_GO/P substrates. Thus, the growth inhibitory activity of these substrates was conserved across all the microbial species with Al_GO100P, Al_GO250P, and Al_GO500P exhibiting a higher inhibitory potential compared to controls (glass and bare Al), whereas Al_GO50P displayed a moderate inhibitory effect.

605 For a comparative analysis, microbial growth inhibition was performed in presence of pristine
606 GO as shown in Supporting Information (Figure S5A). Relative to the activity of GO, the
607 fabricated substrates were shown to exhibit superior antimicrobial potential towards both
608 bacterial and fungal cells. Besides, evaluation of PEDOT:PSS activity revealed no intrinsic
609 antimicrobial potential over a wide concentration range (1 µg/mL, 50 µg/mL, 100 µg/mL, 250
610 µg/mL, 500 µg/mL, 1 mg/mL, and 2 mg/mL) (Figure S5B, Supporting Information). Therefore,
611 the relative efficacy of Al_GO/P substrates could be correlated to varied concentrations of GO
612 on Al_GO/P substrates correlating to earlier literatures[89,90].

613

614

615

616

617

618

619

620

621

622

623

624

625

3.2.2. Al_GO/P substrates demonstrate potent antibiofilm activity

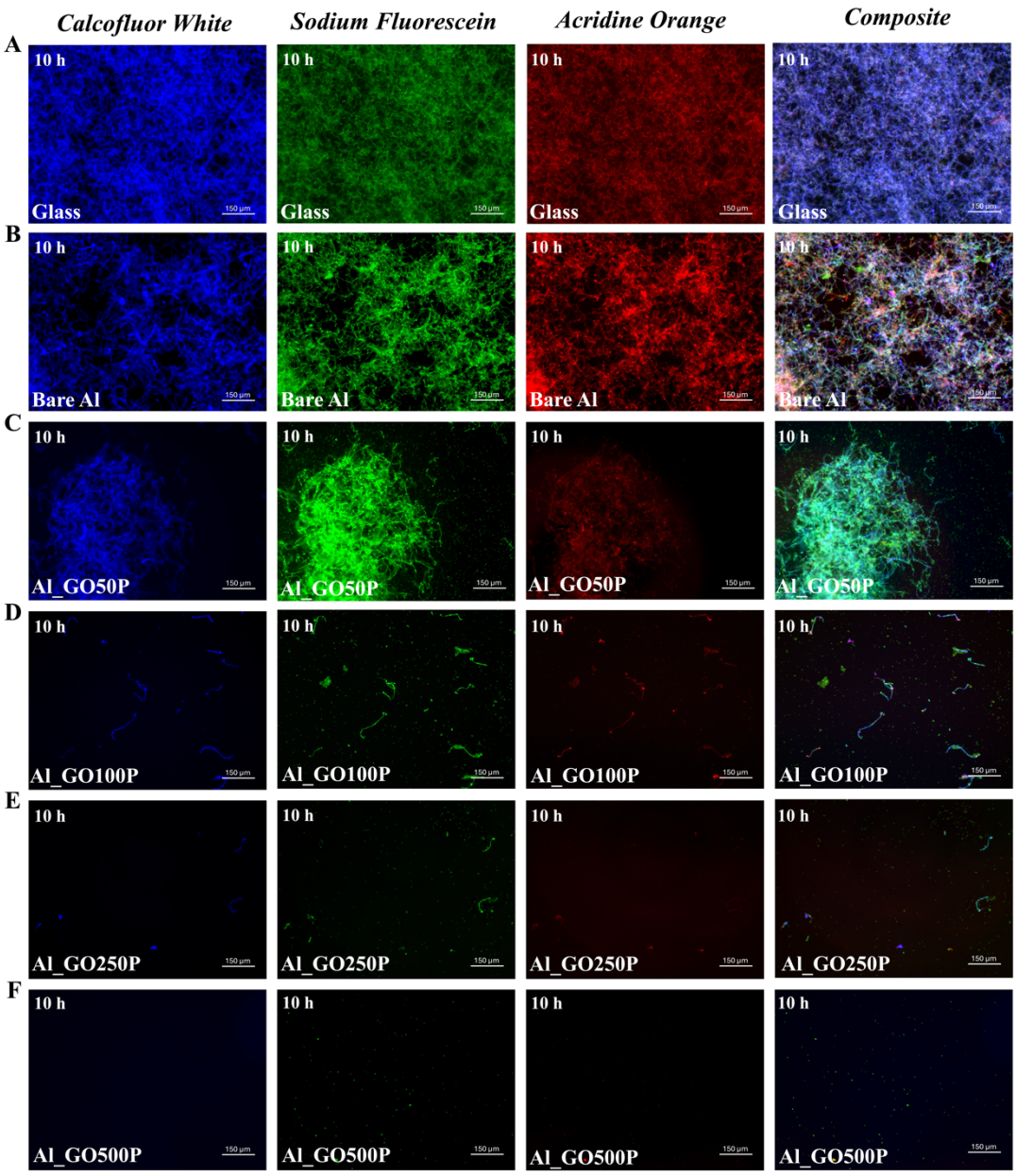

Figure 4. Fluorescence microscopic images of mixed species (*C. albicans*, *S. aureus*, and *E. coli*) biofilm formation (10^7 CFU). Mixed candida-bacterial suspensions were exposed, (**A, B**) to control surfaces (glass and bare Al), and (**C–F**) to various Al_GO/P substrates. Post-exposure, mixed species biofilm were allowed to grow for 10 hours under biofilm stimulating conditions after which the samples were stained with calcofluor white (*blue*), acridine orange (*red*), and sodium fluorescein (*green*) to visualize *C. albicans*, *S. aureus*, and *E. coli*, respectively. Biofilms were imaged using an in-house fluorescence microscope at 40× magnification.

Biofilms are mixed community of microbial population adherent to various biotic and abiotic surfaces[2]. These organized microbial structures play a crucial role in infection dissemination, antibiotic resistance, and may pose a threat to the host's immune system[91]. As previously reported, the antimicrobial efficacy of GO has been well documented across literature[92–95]. In this study, we have evaluated the activity of GO-PEDOT:PSS coated Al (Al_GO/P) surfaces towards mixed species (*Candida*-bacterial) biofilm formation. The antimicrobial activity of the synthesized Al_GO/P surfaces was evaluated against *C. albicans*, *S. aureus*, and *E. coli* by examining the progress of biofilm maturation over a period of 10 hours under biofilm stimulating conditions.

Fluorescent stains were used to visualize Gram-positive *S. aureus* (acridine orange, red), Gram-negative *E. coli* (sodium fluorescein, green), and fungus *C. albicans* (calcofluor white, blue). Control surfaces, such as glass (Figure 4A) and bare Al (Figure 4B), demonstrated dense biofilm formation consisting of bacterial cells within intricate fungal hyphae. This indicates robust microbial colonization on these surfaces that provide a favorable environment for biofilm maturation. On the contrary, significant biofilm inhibition was observed on Al_GO/P substrates. A complete disruption of biofilm structure with only a few adherent microbial cells were noted in presence of Al_GO500P (Figure 4F), closely followed by Al_GO250P (Figure 4E), Al_GO100P (Figure 4D). A moderately inhibited biofilm structure was visualized in presence of Al_GO50P (Figure 4C).

Further to show the robust activity of Al_GO/P, antibiofilm potential was examined at a higher microbial load of 10^8 CFU (Figure S7, Supporting Information). The extent of antibiofilm activity of Al_GO/P substrates were comparable when tested with 10^7 CFU and 10^8 CFU of mixed microbial population. These findings further support the broad-spectrum antimicrobial nature of the Al_GO/P substrates as shown by growth inhibition assay, while substrates with higher GO concentrations yield a more pronounced biofilm inhibitory effect.

682 Next, crystal violet (CV) staining technique was performed to quantitate mixed species (10^7
683 CFU) biofilm formation over various test substrates. Glass was used as a positive growth
684 control exhibiting 100% biofilm formation. It was observed that biofilm biomass was lowest
685 when exposed to Al_GO500P, decreasing significantly to 14.3% ($p < 0.0001$), indicating the
686 highest inhibitory activity among the tested Al_GO/P surfaces (Figure S6 and Table S2,
687 Supporting Information). This was followed by Al_GO250P and Al_GO100P, with biomass
688 reductions to 39.3% and 48.5%, respectively ($p < 0.0001$ for both). The biofilm biomass was
689 reduced to 91.3% ($p > 0.05$) in presence of Al_GO50P, indicating the least inhibitory effect
690 (Figure S6 and Table S2, Supporting Information). A similar result was obtained at higher
691 microbial inoculum load at 10^8 CFU (Figure S8 and Table S2, Supporting Information).

692 Current results highlights a clear correlation between increasing GO concentration on Al
693 surface and its inhibitory effect on biofilm formation. Al_GO50P appears to have a non-
694 significant ($p > 0.05$) role in biofilm inhibition, whereas Al_GO/P substrates with higher
695 concentration of GO (100, 250, and 500 μg/mL) could remarkably inhibit biofilm formation.
696 Besides, a non-significant ($p > 0.05$) inhibition of biofilm formation over bare Al (Figure S6,
697 Figure S8 and Table S2, Supporting information) suggested a superior antibiofilm activity of
698 Al_GO/P surfaces. Additionally in a comparative study, we used GO solutions at corresponding
699 concentrations, which resulted in non-significant ($p > 0.05$) inhibition of biofilm formation
700 relative to control surface glass (Figure S9 and Table S2, Supporting Information). A pairwise
701 analysis of antibiofilm efficacy between pristine GO and test surfaces indicated significant
702 inhibition ($p < 0.0001$) induced by Al_GO/P at corresponding concentration (Figure S10,
703 Supporting Information). The quantitative data for these results at two different inoculum
704 concentrations along with the biofilm inhibitory potential of pristine GO are provided in Table
705 S2, Supporting Information.

Summarizing the results from the growth inhibition (Figure 3) and antibiofilm assays, Al_GO100P, Al_GO250P, and Al_GO500P substrates exhibit superior antimicrobial activity compared to Al_GO50P and control surfaces. This is possibly due to the suppression of microbial colonization and biofilm maturation in the presence of Al_GO/P substrates[44]. Moreover, the lower porosity (Table 3) of Al_GO/P (especially Al_GO100P, Al_GO250P, and Al_GO500P) may have contributed to this enhanced effect, by limiting microbial attachment and biofilm formation. Further analysis via SEM is required to visualize the membrane-damaging (biocidal) activity of Al_GO/P, as demonstrated in the following section.

3.2.3. Al_GO/P substrates induced cell membrane damage in mixed species microbial cell population

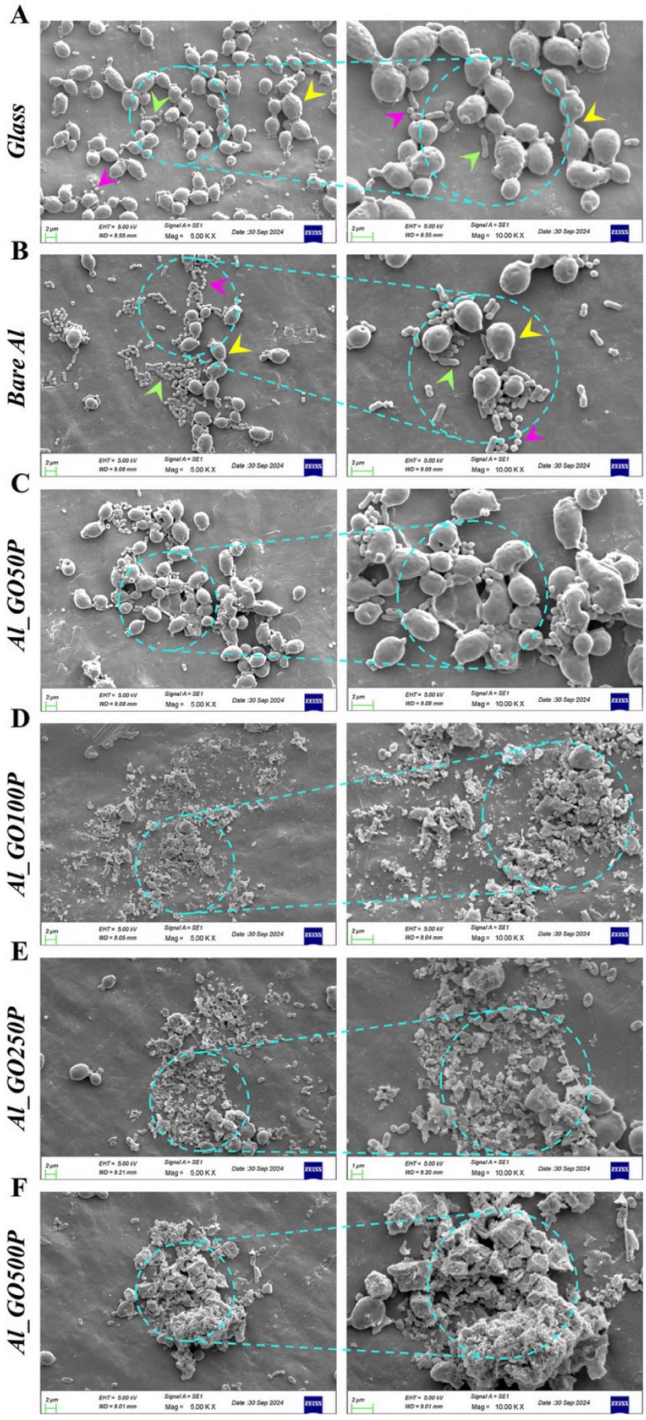

Figure 5. SEM analysis to visualize mixed microbial (*C. albicans*, *S. aureus*, and *E. coli*) cells. Representative SEM micrographs show the morphology of mixed *C. albicans* (*arrowheads, yellow*), *S. aureus* (*arrowheads, pink*), and *E. coli* (*arrowheads, green*) cells after 10 hours of exposure to different control and test substrates: (**A**) Glass, (**B**) Bare Al, (**C**) Al_GO50P, (**D**) Al_GO100P, (**E**) Al_GO250P, and (**F**) Al_GO500P. Images captured at 5000×

and 10,000× magnifications (*dashed circles, cyan*) revealed extensive membrane damage, and complete loss of cellular architecture in microbial cells exposed to Al_GO100P, Al_GO250P and Al_GO500P, compared to the intact morphology observed on control surfaces (Glass, Bare Al). Exposure to Al_GO50P resulted in minor morphological alterations, such as fused and wrinkled cell structures.

In a comprehensive study examining the effects of Al_GO/P surfaces on bacterial and fungal cells, SEM was employed to analyze alterations in cellular architecture and membrane integrity. SEM analysis revealed that cells exposed to the control surfaces (glass, bare Al) maintained their normal cellular morphology, appearing healthy and uniform (Figure 5A and 5B). Exposure to Al_GO50P, displayed less severe but notable morphological damage, including fused cells with wrinkled appearance (Figure 5C). In contrast, exposure to the Al_GO100P (Figure 5D), Al_GO250P (Figure 5E), and Al_GO500P (Figure 5F) induced significant damage to cell membrane with complete loss of cellular architecture for all (*C. albicans*, *S. aureus*, and *E. coli*) cell types. The study demonstrated consistent biocidal activity of the test substrates (Al_GO100P, Al_GO250P, Al_GO500P) towards a mixed microbial population consisting of Gram-positive and Gram-negative bacteria, as well as fungi.

The enhanced antimicrobial potential including biocidal activity of Al_GO/P can be correlated to superior surface hydrophobicity at higher GO concentrations (Table 2 and Figure S2, Supporting Information). This may have facilitated sustained interactions between the microbial cell wall and the Al_GO/P surface, thereby compromising membrane integrity[96]. Besides, we cannot exclude the possibility of electron transfer events occurring in a conductive background of the Al_GO/P substrates, which may lead to the generation of reactive oxygen species (ROS), as shown in previous literature[44,50]. Next, we investigated ROS generation at the substrate interface and intracellularly to further validate the underlying inhibitory mechanism of the Al_GO/P substrates.

3.2.4. Al_GO/P substrates induce intracellular and surface ROS production

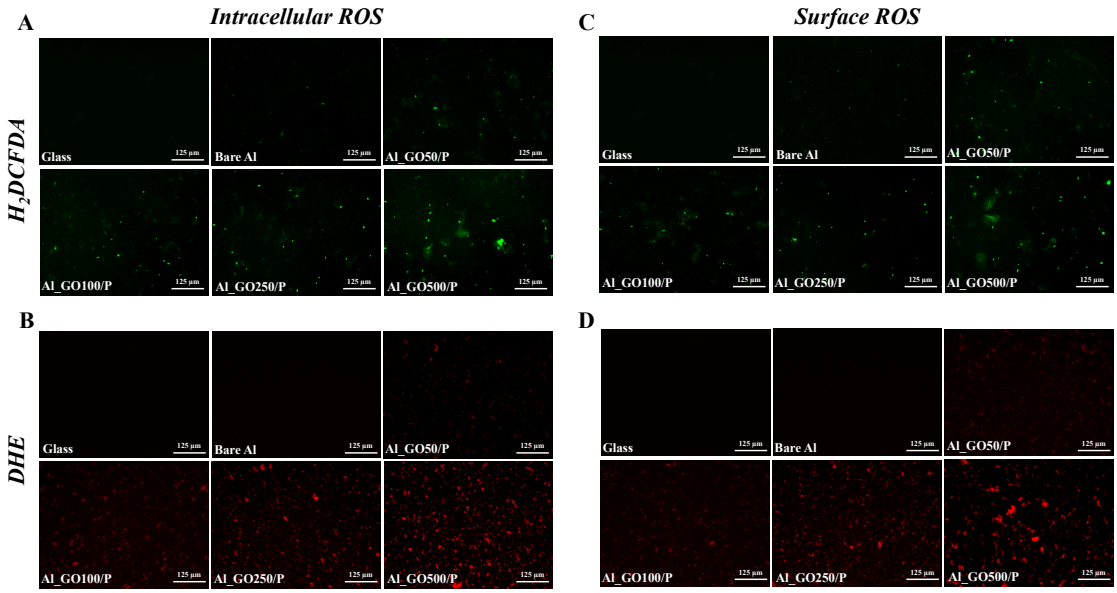

Figure 6. Evaluation of (A, B) intracellular, and (C, D) surface ROS production on Al_GO/P substrates using H_2DCFDA and DHE dye. Following exposure to various test and control surfaces **(A)** Mixed microbial cell population (*C. albicans*, *S. aureus*, and *E. coli*) were stained with H_2DCFDA dye (green cells), and **(B)** mixed bacterial cells consisting of *S. aureus* and *E. coli* were stained with DHE dye (red cells), for detection of intracellular ROS production. No ROS production was observed on glass, and only minimal signal was detected on Al relative to the test substrates. Abundant fluorescent signals correlating to intracellular ROS generation were observed for the bacterial and fungal cells exposed to Al_GO500P, Al_GO250P, and Al_GO100P surfaces using H_2DCFDA (green) and DHE (red) fluorescent dyes. Al_GO50P induced relatively lesser number of fluorescent cells; Detection of ROS production on the surface of Al_GO/P substrates after a 10-hour of exposure to **(C)** mixed population of cells (*C. albicans*, *S. aureus*, and *E. coli*) using H_2DCFDA dye (green fluorescence), and **(D)** mixed bacterial cells (*S. aureus* and *E. coli*) with DHE dye (red fluorescence). ROS indicator dyes H_2DCFDA and DHE were applied on different test and control surfaces. No ROS production was noticed on the surface of Glass and Al relative to test substrates. Varied levels of abundant fluorescent signals correlating to ROS generation were observed on the surface of Al_GO500P, Al_GO250P, and Al_GO100P as revealed by H_2DCFDA (green) and DHE (red) stains. Relatively mild signal was detected on the surface of Al_GO50P. Cells were imaged using in-house fluorescence microscope at 40× magnification.

The catalytic generation of ROS at metal-environment interfaces is a well-characterized process, mediated by physicochemical interactions that promote oxidative stress conditions[97,98]. These interactions involve complex mechanisms, including redox reactions

820 and surface modifications, which could mediate the transfer of electrons and lead to the
821 formation of ROS[50]. The production of ROS can have significant implications for both the
822 metal surfaces and the biological systems they interact with, potentially affecting cellular
823 responses[97]. In this work, ROS production was evaluated using the indicator dye 2',7'-
824 dichlorodihydrofluorescein diacetate (H_2DCF-DA) after exposing mixed (bacterial and fungal)
825 microbial cells to various Al_GO/P substrates. This dye is effective in detecting a wide range
826 of ROS, including hydrogen peroxide (H_2O_2), hydroxyl radicals (•OH), and other reactive
827 species such as carbonate radicals and nitric oxide[99]. When ROS are present, the initially non-
828 fluorescent H_2DCF-DA is transformed into the highly fluorescent compound 2',7'-
829 dichlorofluorescein (DCF+), which emits a green signal observable through fluorescence
830 microscopy.

831 In addition, dihydroethidium (DHE) is also utilized for ROS detection. DHE displays blue
832 fluorescence in the cell cytoplasm; however, upon reacting with superoxide anions, it is
833 oxidized to form 2-hydroxyethidium, which intercalates into DNA and exhibits red
834 fluorescence (DHE+). This makes DHE particularly useful for detecting cytosolic superoxide
835 (O_2•$^-$)[99]. It can also undergo nonspecific oxidation by other radicals like peroxynitrite
836 (ONOO−) and hydroxyl radicals (•OH). In this work, H_2DCFDA dye was employed to assess
837 the overall oxidative stress levels in mixed *Candida*-bacterial cell suspensions. Additionally,
838 DHE was utilized specifically to detect cytosolic superoxide in the mixed bacterial cell
839 suspensions (*S. aureus* and *E. coli*).

840 We observed that Al_GO/P substrates, especially Al_GO500P, Al_GO250P, Al_GO100P
841 exhibited a significantly higher number of DCF+ signals indicative of elevated ROS relative
842 to control surfaces both intracellularly (Figure 6A) and at the substrate surface (Figure 6C) in
843 mixed pathogen populations consisting of *S. aureus*, *E. coli*, and *C. albicans*. This was closely
844 followed by Al_GO50P displaying relatively lower number of DCF+ fluorescent cells. The

control Al surface showed minimal DCF+ signal, while the glass surface displayed no detectable DCF+ (green) signal at all. The elevated ROS levels may directly correlate to an electron transfer event from the microbial cells to the GO functional groups over conductive substrates causing surface ROS production. Elevated intracellular ROS production is indicative of cell death and the activation of related cell signaling pathways[100].

We further examined the presence of cytosolic superoxide in a mixed bacterial population both intracellularly (Figure 6B) and at the substrate interface (Figure 6D). Similar to our observation in Figure 6A and 6C, control surfaces such as glass and bare aluminium, did not exhibit any DHE+ (red) cells, indicating a lack of ROS production overall. Conversely, varying numbers of fluorescent DHE+ cells were observed on different Al_GO/P substrates. Notably, Al_GO500P, Al_GO250P, and Al_GO100P induced a higher population of DHE+ cells than Al_GO50P. It is plausible that extending the exposure time on the substrate surface may lead to a greater number of ROS-positive cells.

Previous studies have highlighted the role of ROS in the broad-spectrum antimicrobial activity of graphene and its derivatives[44,101]. In fact, oxidative stress can lead to oxidation of proteins, lipids, and nucleic acids in microbial cells, resulting in irreversible membrane damage and cell death[102]. The pronounced microbiocidal activity observed for Al_GO100P, Al_GO250P, and Al_GO500P substrates can be attributed to the conductivity of these substrates (Table 2), which facilitates electron transfer from the microbial cells to the GO surface, and enhanced ROS production. Besides higher surface hydrophobicity values for these substrates (Table 2), may have promoted a stable microbial interaction causing contact mediated membrane damage and ROS induced stress. Although Al_GO50P exhibited higher conductivity, its antimicrobial performance was less, likely due to its lower surface hydrophobicity, causing an attenuated microbial cell interaction with its surface.

869 **3.3. Assessment of anticorrosion potential of Al_GO/P substrates**

870 *3.3.1. Al_GO/P substrates exhibit biocorrosion resistance*

871 The corrosion rate of the fabricated Al_GO/P substrates was primarily assessed in two
872 designated immersion systems, as detailed in the experimental section. Our objective was to
873 analyse the corrosion kinetics of these materials in an abiotic system, which consisted solely
874 of growth media and antibiotics to inhibit any microbial growth. This setup allowed us to
875 evaluate the chemical corrosion properties of Al_GO/P surfaces in a controlled environment,
876 free from biological contamination. Parallelly, we investigated a biotic system that included
877 microbial cells to assess microbiologically influenced corrosion (MIC) potential of Al_GO/P
878 substrates. This dual approach not only provides a comprehensive understanding of the
879 corrosion behaviour of the fabricated Al_GO/P substrates but also highlights their potential
880 effectiveness in real-world applications, where both chemical (abiotic) and biological (biotic)
881 factors influence corrosion rates[103]. In addition to evaluating the synthesized Al_GO/P
882 substrates, we included two control materials in this study: bare aluminium, and cold-rolled
883 steel (CR Steel), which is recognized as a highly corrosive material and serves as a control in
884 corrosion studies due to its known susceptibility to corrosion[104]. Although both chemical
885 corrosion and MIC involve material degradation, chemical corrosion generally proceeds faster
886 and more aggressively due to its direct chemical interactions with the metal surface, especially
887 in high-temperature or harsh environments[105]. Whereas MIC, also an electrochemical process,
888 relies on the activity of microorganisms and their metabolites to promote corrosion, often under
889 specific conditions[25].

890

891

892

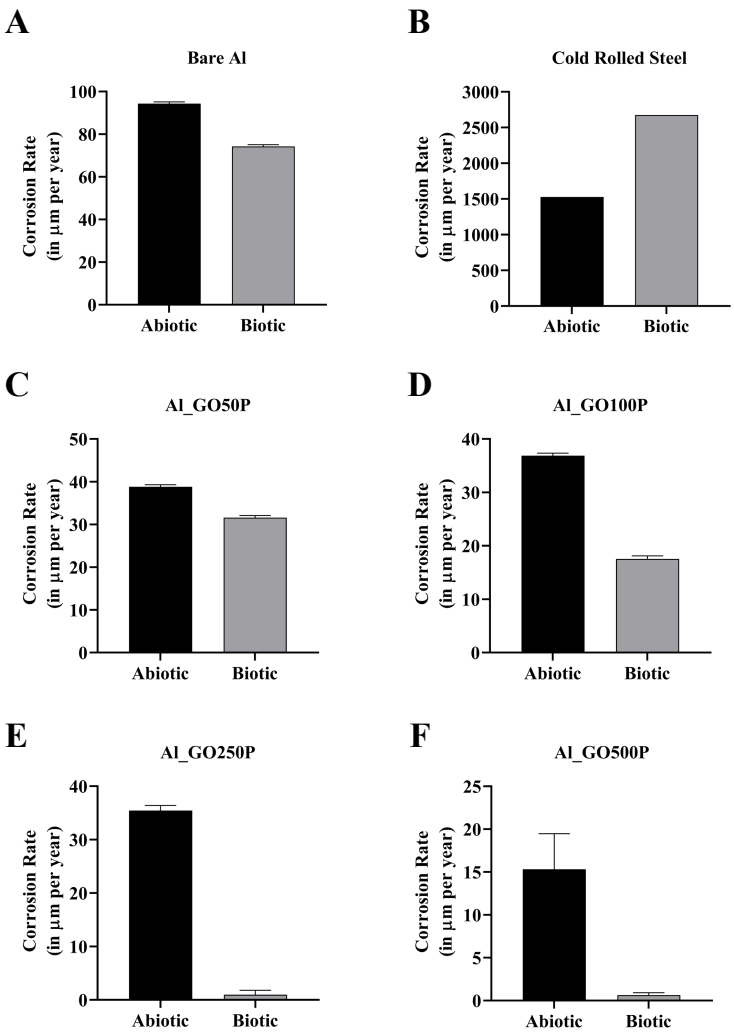

Figure 7. Corrosion rates of various control and Al_GO/P substrates in µm per year after 45 days of exposure to abiotic and biotic environments. Results show Al_GO/P substrates, particularly Al_GO500P and Al_GO250P, closely followed by Al_GO100P and Al_GO50P, exhibited significantly lower corrosion rates compared to control surfaces (bare Al and CR steel), indicating enhanced resistance to MIC. Error bars represent ±1 standard deviation (SD) from mean for three independent biological replicates (n=3).

Figure 7 illustrates the corrosion rates of various substrates after 45 days of immersion in the studied systems, highlighting the effects of both abiotic and biotic conditions. In the abiotic system, the corrosion rates were measured as follows: 94.3 ± 0.8 µm/year for aluminium

(Figure 7A), 1528.3 ± 0.1 μm/year for CR Steel (Figure 7B), 38.8 ± 0.5 μm/year for Al_GO50P (Figure 7C), 36.9 ± 0.5 μm/year for Al_GO100P (Figure 7D), 35.4 ± 1.0 μm/year for Al_GO250P (Figure 7E), and 15.3 ± 4.1 μm/year for Al_GO500P (Figure 7F). In contrast, the corrosion rates in the biotic system were recorded as follows: 74.2 ± 0.8 μm/year for aluminium (Figure 7A), 2674.2 ± 0.3 μm/year for CR steel (Figure 7B), 31.6 ± 0.5 μm/year for Al_GO50P (Figure 7C), 17.6 ± 0.6 μm/year for Al_GO100P (Figure 7D), 1.0 ± 0.8 μm/year for Al_GO250P (Figure 7E), and 0.6 ± 0.3 μm/year for Al_GO500P (Figure 7F). It was noted that, in general, the immersion systems lacking microbial presence tended to display higher corrosion rates. However, this trend did not apply to CR steel, which is a known corrosive material used as a control in this study and inherently exhibits high corrosion rates. This observation aligns with the understanding that chemical corrosion often occurs at a faster and higher rate than MIC, which is primarily driven by electrochemical reactions in aggressive environments, as mentioned by previous literatures[105–107]. Conversely, the immersion system with microbial load showed a lower corrosion rate, reflecting the variability of MIC, which can be influenced by factors such as the type of microorganisms present and their metabolic by products[24,25]. Corrosion rates for the Al_GO/P substrates immersed in the abiotic system corresponded to a moderate corrosion intensity as defined by the NACE Standard RP-07-75[67].

Similarly, in the biotic system, Al_GO/P substrates, particularly Al_GO500P and Al_GO250P, followed by Al_GO100P and Al_GO50P, exhibited significantly lower corrosion rates compared to the control surfaces (bare Al and CR steel), indicating enhanced resistance to MIC. It can be inferred that increasing GO concentration(s) in coatings enhances biocorrosion resistance in Al_GO/P system, likely attributable to enhanced barrier characteristics and reduced microbial adhesion[108–111]. These findings are further supported by results from the antibiofilm assays (Figure 4, Figure S6 and Table S2, Supporting Information) and SEM

analysis (Figure 5), which collectively demonstrate enhanced antimicrobial efficacy and contact-mediated cell membrane damage at higher GO concentrations.

Next, FESEM analysis revealed distinct morphological alterations in control samples (bare Al and CR Steel) compared to the synthesized Al_GO/P substrates following immersion under abiotic (Figure S11, Supporting Information) and biotic (Figure S12, Supporting Information) conditions. These observations align with the corrosion rate analyses (Figure 7), underscoring the superior anticorrosion performance of the GO-PEDOT:PSS functionalized Al system. In contrast, uncoated bare Al and CR Steel exhibited pronounced localized pitting and deep corrosion features, suggesting their susceptibility towards corrosion. The optical images of the control and test substrates before and after immersion in abiotic and biotic environments are presented in Figure S13 (Supporting Information).

Overall, these results underscore the critical role of GO-PEDOT:PSS coating concentration in improving the corrosion resistance of Al substrates in both abiotic and biotic immersion environments. Given that corrosion products are known to directly contribute to cytotoxic effects on human cells[26], and considering the promising corrosion resistance observed in Al_GO/P surfaces, we evaluated the biocompatibility of the Al_GO/P substrates in the upcoming section.

3.4. Cytotoxicity assessment: Al_GO50P and Al_GO100P demonstrate superior biocompatibility

MTT assay is a widely utilized method for assessing cell viability and proliferation, relying on the metabolic activity of living cells[70,112]. This assay involves the reduction of the yellow tetrazolium salt, MTT (3-(4,5-dimethylthiazol-2-yl)-2,5-diphenyltetrazolium bromide), to an insoluble purple formazan product by mitochondrial enzymes present in metabolically active

cells. The amount of formazan produced is directly proportional to the number of viable cells in the sample, allowing for quantification through absorbance measurements at 570 nm.

For biocompatibility assessment, Al_GO1000P, featuring a GO concentration of 1 mg/mL, was included for comparative analysis[44]. We conducted MTT assay with material extracts as well as direct exposure to the substrates to gain a comprehensive understanding of their effects on HEK293T kidney cell lines[113,114]. Given that the release of nanomaterials from antimicrobial surfaces poses a significant concern, potentially leading to systemic toxicity affecting various organs and functional systems, it was crucial to investigate this further[27]. An extract test was performed on control and Al_GO/P substrates to determine whether any substance was leaching from the surface into the growth medium[71]. The cell viability values used to plot the graphs are tabulated in Table S3A and S3B (Supporting information) for indirect (extract) and direct contact assay, respectively.

The assessment of cell viability after exposure to the Al_GO/P material extracts (Al_GO50P, Al_GO100P, Al_GO250P, Al_GO500P, Al_GO1000P) revealed non-significant ($p > 0.05$) impact on cell growth or viability when compared to the control HEK293T cells in growth media alone (Figure 8A and Table S3A, Supporting Information). No changes in HEK293T cell viability were observed upon indirect contact with the glass surface, as anticipated. In contrast, extracts from bare aluminum resulted in a notable decrease in HEK293T cell viability, dropping to 71.9% ($p \leq 0.0001$) and 72.6% ($p \leq 0.0001$) at 24 and 48 hours, respectively; compared to unexposed control cells, which exhibited a viability of 100% at similar time points. As shown by previous literatures, the systemic toxicity concern arises from the ability of bare aluminum to release ions or particles that can disrupt cellular function, leading to reduced viability and potential long-term health effects[115,116]. Current results suggested that fabricated Al_GO/P substrates possess a stable GO-PEDOT:PSS coating, effectively minimizing the risk of harmful leaching and subsequent toxicity.

Additionally, direct contact assay was conducted to validate uses of Al_GO/P substrates for potential *in vivo* biomedical applications. Cell viability data presented in Figure 8B and Table S3B, Supporting Information, indicate that exposure to Al_GO50P (89.5% at 24 h and 95.8% at 48 h; $p > 0.05$) and Al_GO100P (90.9% at 24 h and 96.1% at 48 h; $p > 0.05$) resulted in no significant change in HEK293T cell viability compared to the control. In contrast, Al_GO250P (86.7% at 24 h, $p > 0.05$; 84.3% at 48 h, $p = 0.0116$) and Al_GO500P (82.5% at 24 h, $p = 0.0234$; 84.1% at 48 h, $p = 0.0108$) showed a moderate reduction in cell viability over 24-48 hour. Notably, Al_GO1000P (64.9% at 24 h, $p < 0.0001$; 59.1% at 48 h, $p < 0.0001$) caused a significant decrease in HEK293T cell viability. HEK293T cells exposed to bare Al demonstrated similar loss in cell viability percentage, 77.5% at 24 hours ($p = 0.0038$) and 53% at 48 hours ($p < 0.0001$). As expected there was no alteration in the viability of HEK293T cells in direct contact with the glass surface. These results collectively highlight the superior biocompatibility of Al_GO50P and Al_GO100P, underscoring their potential for possible biomedical applications. We also conducted comparative studies on the HEK293T cell viability exposed to pristine GO and PEDOT:PSS at corresponding concentrations. The cell viability percentage(s) decreased with increasing concentration(s) of pristine GO and PEDOT:PSS (Figures S14 and S15, Supporting Information) when exposed to HEK293T cells for a period of 24 and 48 hours. Further, PEDOT:PSS at a concentration used to prepare the hybrid coating in this study (1 μg/mL) led to nonsignificant alteration in the HEK293T cell viability.

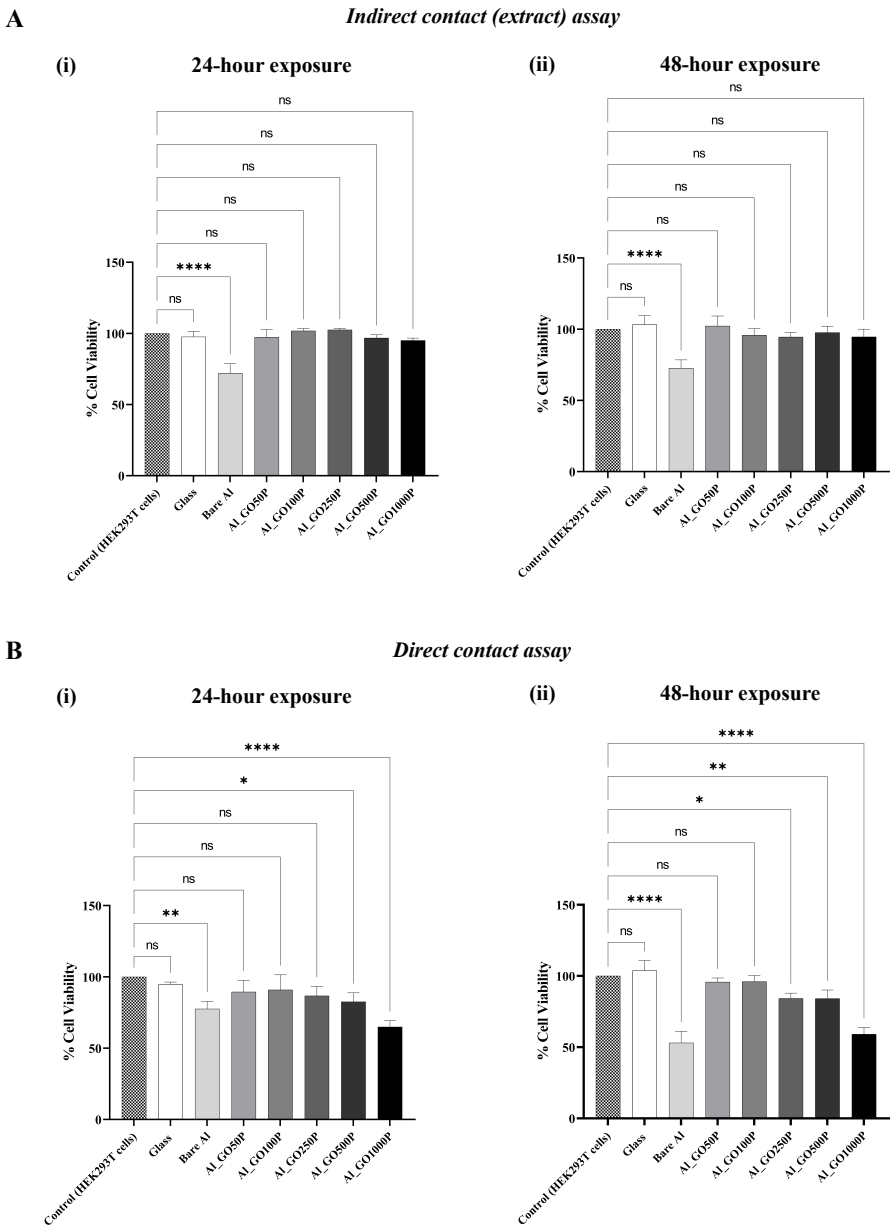

Figure 8. Cytotoxicity evaluation of control and Al_GO/P substrates. Comparison of cell viability, assessed by MTT method in the DMEM culture medium, after exposure to (**A**) Al_GO/P sample extracts by indirect contact assay and (**B**) after direct contact with the Al_GO/P samples; at (**i**) 24-hour and (**ii**) 48-hour. Data are expressed as % values of result obtained in comparison to control cells (HEK293T) not exposed to materials or material extracts. Results from indirect contact assay showed Al_GO/P substrates maintained optimal biocompatibility compared to bare Al over 48 hours. While direct contact assay indicated high cell viability for Al_GO50P and Al_GO100P, with Al_GO250P showing minor viability changes at 48 hours, while significant decreases were observed for Al_GO500P and Al_GO1000P over 48 hours. Error bars represent ±1 standard deviation (SD) from mean for

three independent biological replicates (n=3). Statistical significance was assessed using one-way ANOVA; specific p-values of <0.05, <0.01, <0.001, and <0.0001 were indicated as *,**,***, and ****, respectively.

Current findings confirm that Al_GO/P surfaces do not exhibit leaching, as evidenced by the extract (indirect) assay. HEK293T cells exposed to extracts from all Al_GO/P test surfaces maintained viability comparable to the untreated control group, whereas extracts from bare aluminium caused a significant reduction in cell viability. The corrosion resistance properties of the Al_GO/P substrates may have minimized the cytotoxicity effects associated with leaching, as reported in prior literature[117,118]. Additionally, direct contact assays showed that HEK293T cells retained normal viability on Al_GO50P and Al_GO100P surfaces, with no statistically significant differences from the controls. In contrast, direct exposure to bare Al ($p < 0.0001$), Al_GO500P ($p = 0.0108$), and Al_GO1000P ($p < 0.0001$) surfaces resulted in marked decrease in cell viability over a period of 48 hours. Al_GO250P did not influence cell viability over 24 hour of exposure time, however induced minor alteration in viability ($p < 0.05$) after 48 hour of exposure. While Al_GO250P and Al_GO500P exhibited remarkable antibiofilm properties, their negative effect on cell viability suggests potential cytotoxicity concerns in direct-contact mediated biomedical applications. Therefore, these surfaces may be more suitable for *in vitro* or exterior uses where robust antimicrobial activity is essential. Although, Al_GO50P demonstrated excellent biocompatibility, it lacked significant antimicrobial, and antibiofilm efficacy (Figure 4), indicating a need for further optimization to enhance its performance. Overall, Al_GO100P achieved a desirable balance, combining both high biocompatibility and effective antibiofilm activity, and thus stands out as a promising candidate for *in vivo* biomedical device applications where cellular compatibility and biofouling resistance are paramount.

In summary, the results underscore the broader potential of GO-PEDOT:PSS hybrid coatings on bare Al sheets in healthcare setup. By enhancing biocorrosion resistance and antibiofouling activity, GO-PEDOT:PSS coatings on Al serve as an effective barrier against microbial colonization, which is known to accelerate MIC. The capacity of Al_GO/P substrates to decelerate Al corrosion rates (Figure 7) highlights their potential as versatile materials for biomedical devices such as orthopedic implants, dental fixtures, cardiovascular stents; where sterility and tissue healing are critical requirements[24,25]. Continued research into the interactions between graphene-based materials and biological systems will be vital for optimizing their use in medical as well as industrial sectors while enhancing material safety and efficacy.

4. Conclusion

Biofilms are implicated in 60–70% of nosocomial infections and significantly increase the risk of medical device-associated complications, leading to higher infection rates, morbidity, and mortality in clinical settings[119]. The resilience of biofilms to conventional antibiotics underscores the urgency for innovative surface technologies that can effectively prevent microbial colonization and reduce HAIs. Considering these challenges, there is a critical need to design and evaluate novel materials possessing broad-spectrum antifouling capabilities, minimizing cytotoxicity and biocorrosion. This systematic assessment is essential to ensure that the fabricated materials are effective in inhibiting the growth of pathogens while being safe for both *in vitro* and *in vivo* environments.

Understanding the basis of material degradation becomes particularly important when addressing the phenomenon of MIC. MIC represents an intersection where biotic and abiotic factors converge to accelerate material degradation through complex bio-electrochemical

processes[24,105]. Apart from electrochemical corrosion process, microbial metabolites containing organic acids, carboxyl groups, lower the pH of the metallic environment accelerating corrosion[120]. Prior research demonstrates that biofilm formation on metal surfaces can alter the microenvironment and cause an increased corrosion rate[121,122]. Extensive scientific literature demonstrates that metal corrosion results from synergistic interactions of multiple mechanisms rather than a single pathway, with biocorrosion operating in tandem with chemical corrosion processes to accelerate material degradation[25,121–123]. Moreover, aluminum alloys are particularly susceptible to MIC due to their inherent tendency to form passive oxide layers, which can be compromised by microbial metabolites leading to localized pitting and crevice corrosion[124]. The incorporation of PEDOT:PSS was strategically chosen due to its ability to form adherent films that enhance the mechanical integrity and conductivity of the Al_GO/P surface which may also provide additional barrier properties against corrosive species[125].

Building upon this understanding, our experimental approach focused on comprehensive antifouling evaluation. Evaluation of microbial attachment to the synthesized Al_GO/P substrates was evaluated via growth inhibition assay suggesting superior antimicrobial properties of Al_GO100P, Al_GO250P, and Al_GO500P compared to Al_GO50P and bare Al. Extensive antibiofilm assays via fluorescence microscopy along with quantitative studies concluded similar observations. These findings were further substantiated through advanced microscopic (SEM) analysis confirming the biocidal nature of the coated substrates.

Given the promising antimicrobial results, it was essential to evaluate the practical performance of Al_GO/P in real world scenario by evaluating the biocorrosion resistance properties under abiotic and biotic immersion environments. Analyses from corrosion rates (Figure 7) and FESEM imaging (Figures S11 and S12, Supporting Information) revealed that the substrates exhibited biocorrosion resistance in the order; Al_GO500P, Al_GO250P, Al_GO100P, and

Al_GO50P compared to controls (bare Al and CR Steel). The improved corrosion resistance of Al_GO/P surfaces may be attributed to their reduced porosity (Table 3), which results in decreased microbial contamination and, consequently, a lower MIC (Figure 7, Figures S11 and S12, Supporting Information)[44,88].

Next, it was crucial to conduct biocompatibility testing to ensure the safety and suitability of Al_GO/P within physiological environment. Al_GO100P was identified as a promising candidate for *in vivo* implant material, owing to its excellent biocompatibility (Figure 8) along with remarkable antibiofilm (Figure 4) and anticorrosion properties (Figure 7 and Figures S11 and S12, Supporting Information). Al_GO250P demonstrates favorable biocompatibility profile at 24 hours and minimal viability loss at 48 hours, suggesting potential suitability for short-term biomedical applications. In contrast, the reduced cell viability observed with Al_GO500P and Al_GO1000P suggests a potential for cytotoxicity, making them better suited for *ex vivo* applications. The toxic effects of aluminum (Al^{3+}) result from its ability to disrupt cellular homeostasis through multiple mechanisms, including oxidative stress induction, enzymatic inhibition, and direct cellular membrane damage[115]. The overall enhanced HEK293T cell viability observed in both indirect and direct contact assays indicated that GO-PEDOT:PSS hybrid coating may effectively reduce Al-related cytotoxicity while preserving the biocompatibility essential for biomedical applications.

As reported earlier, the membrane-damaging activity of GO involves multiple mechanisms, such as nano-knife or sharp-edge effects, membrane pore formation, phospholipid extraction, and electron extraction by GO side groups, which induce oxidative stress[36]. In the current study, the synthesized Al_GO/P system can provide active antimicrobial mechanisms preventing the attachment of microbial cells that typically drive localized pitting corrosion in aluminum alloys that affects material longevity. To gather a clear mechanistic understanding and to correlate cell membrane damage due to possible electron extraction events, we

conducted intracellular and surface ROS production assay. The presence of intracellular ROS indicates microbial cell death, whereas the detection of ROS on the Al_GO/P surface points to an interface phenomenon that confirms electron transfer directed ROS generation over the conductive Al_GO/P substrates.

Summarizing the experimental data, we discuss a mechanistic model underlying the robust antimicrobial and antibiofilm activity of the fabricated Al_GO/P substrates (Al_GO100P, Al_GO250P, and Al_GO500P) (Figures 3 and 4). Firstly, surface hydrophobicity of the Al_GO/P substrates promotes stable interactions with microbial cells, which likely facilitates contact-mediated membrane disruption through interaction with GO (Table 2). In addition, the conductive nature (Table 2) of the synthesized substrates may have induced electron transfer events that generate ROS (Figure 6), further contributing to microbial cell damage (Figure 5). Notably, these surfaces were also found to possess fewer porous domains (Table 3) relative to bare Al, which limits microbial colonization resulting in a robust antibiofilm activity[88]. Together, these physical and electrochemical interactions might have synergistically enhanced the antibiofouling efficacy of fabricated Al_GO/P surfaces. The superior antibiofouling activities observed for test substrates; Al_GO500P, Al_GO250P, Al_GO100P relative to Al_GO50P can be linked to higher surface hydrophobicity, lower porosity, and higher ROS production (Figure 6, Table 2, Table 3, Figures S2-S4, Supporting Information). Experimental evaluation by utilizing suitable control surfaces like glass, bare Al and pristine GO further ascertain the superior broad-spectrum antibiofouling activity of synthesized Al_GO/P substrates.

In toto, the findings from this study may establish a strong foundation for practical implementation of GO-PEDOT:PSS hybrid coated Al substrates. The synthesized hybrid substrates may provide a promising approach for improving the durability and performance of Al; particularly where corrosion resistance, antibiofouling properties, and biocompatibility are

crucial, such as in the health-care, water treatment, and varied industrial sectors, where MIC plays detrimental roles. Further research and optimization of the Al_GO/P composite system could facilitate the development of advanced aluminum-based materials specifically tailored for healthcare applications, particularly in the design of next-generation biomedical implants with improved material lifespan.

Author Contributions

S.S.N., Conceptualization; Methodology; Validation; Formal analysis; Investigation; Resources; Data curation; Writing original draft; Writing review and editing; Visualization. **R.E.A.**, Conceptualization; Validation; Formal analysis; Writing original draft; Writing review and editing. **A.K.R.,** Investigation; Writing review and editing; **T.N.N.**, Conceptualization; Validation; Formal analysis; Resources; Writing original draft; Writing review and editing. **S.N.**, Conceptualization; Methodology; Validation; Formal analysis; Investigation; Resources; Writing original draft; Writing review and editing; Supervision; Project administration; Funding acquisition.

Acknowledgements

Aluminum substrates were provided by NALCO India, Ltd. The authors gratefully acknowledge the School of Basic Sciences at IIT Bhubaneswar for granting access to their facilities for substrate synthesis and porosity evaluation. Sincere thanks are extended to the central facilities at TIFR Hyderabad for their valuable support in the characterization of Al_GO/P substrates. The authors also appreciate the Central Research Facility at KIIT-DU, Bhubaneswar, for providing access to the scanning electron microscope (SEM). The infrastructure grant from the Department of Biotechnology, Government of India, under the Boost to University Interdisciplinary Life Science Departments for Education and Research (BUILDER) program at KIIT School of Biotechnology is also duly acknowledged. S.S.N. was supported by DD Innovation Incorporated, U.S.A. (Ref No: DD/KIIT/001/2023).

Conflict of Interest Statement

The authors declare that they have no conflict of interest.

Data Availability Statement

All data sources are cited within this article and its Supporting Information.

References

[1] N. C. Bamford, C. E. Macphee, N. R. Stanley-Wall, *Microbiology (United Kingdom)* **2023**, *169*, 001338, DOI: 10.1099/MIC.0.001338.

[2] L. Karygianni, Z. Ren, H. Koo, T. Thurnheer, *Trends Microbiol* **2020**, *28*, 668, DOI: 10.1016/J.TIM.2020.03.016.

[3] HAIs: Reports and Data | HAIs | CDC, *https://www.cdc.gov/healthcare-associated-infections/php/data/index.html*, accessed May 5, **2025**.

[4] L. Guarente, C. Mosconi, M. Cicala, C. De Santo, F. Ciccacci, M. Carestia, L. Emberti Gialloreti, L. Palombi, G. Quintavalle, D. Di Giovanni, E. Buonomo, S. Moramarco, F. Riccardi, S. Orlando, *Infection Prevention in Practice* **2024**, *6*, 100391, DOI: 10.1016/J.INFPIP.2024.100391.

[5] A. Cassini, D. Plachouras, T. Eckmanns, M. Abu Sin, H. P. Blank, T. Ducomble, S. Haller, T. Harder, A. Klingeberg, M. Sixtensson, E. Velasco, B. Weiß, P. Kramarz, D. L. Monnet, M. E. Kretzschmar, C. Suetens, *PLoS Med* **2016**, *13*, e1002150, DOI: 10.1371/JOURNAL.PMED.1002150.

[6] Healthcare-associated infections in European hospitals (PPS survey) 2022-2023, *https://www.ecdc.europa.eu/en/publications-data/healthcare-associated-infections-european-hospitals-pps-survey-2022-2023*, accessed May 5, **2025**.

[7] Each year, 4.3 million patients in hospitals in the EU/EEA are affected by healthcare-associated infections, *https://www.ecdc.europa.eu/en/news-events/each-year-43-million-patients-hospitals-eueea-are-affected-healthcare-associated*, accessed May 5, **2025**.

[8] R. M. Klevens, J. R. Edwards, C. L. Richards, T. C. Horan, R. P. Gaynes, D. A. Pollock, D. M. Cardo, *Public Health Reports* **2007**, *122*, 160, DOI: 10.1177/003335490712200205.

[9] Global report on infection prevention and control 2024, *https://www.who.int/publications/i/item/9789240103986*, accessed May 5, **2025**.

[10] HAI National Action Plan, *https://www.hhs.gov/oidp/topics/health-care-associated-infections/hai-action-plan/index.html*, accessed May 5, **2025**.

[11] P. Mathur, P. Malpiedi, K. Walia, P. Srikantiah, S. Gupta, A. Lohiya, A. Chakrabarti, P. Ray, M. Biswal, N. Taneja, P. Rupali, V. Balaji, C. Rodrigues, V. Lakshmi Nag, V. Tak, V. Venkatesh, C. Mukhopadhyay, V. Deotale, K. Padmaja, C. Wattal, S. Bhattacharya, T. Karuna, B. Behera, S. Singh, R. Nath, R. Ray, S. Baveja, B. A. Fomda, K. Sulochana Devi, P. Das, N. Khandelwal, P. Verma, P. Bhattacharyya, R. Gaind, L. Kapoor, N. Gupta, A. Sharma, D. VanderEnde, V. Siromany, K. Laserson, R. Guleria, R. Malhotra, O. Katoch, S. Katyal, S. Khurana, S. Kumar, R. Agrawal, K. Dev Soni, S. Sagar, N. Wig, P. Garg, A. Kapil, R. Lodha, M. Sahu, M. C. Misra, M. Lamba, S. Jain, H. Paul, J. Sarojini Michael, P. Kumar Bhatia, K. Singh, N. Gupta, D. Khera, D. Himanshu, S. Verma, P. Gupta, M. Kumar, M. Pervez Khan, S. Gupta, V. Kalwaje Eshwara, M. Varma, R. Attal, S. Sudhaharan, N. Goel, S. Saigal, S. Khadanga, A. Gupta, M. A. Thirunarayan, N. Sethuraman, U. Roy, H. Jyoti Raj, D. D'Souza, M. Chandy, S. Mukherjee, M. Kumar Roy, G. Goel, S. Tripathy, S. Misra, A. Dey, T. Misra, R. Ranjan Das, G. Bashir, S. Nazir, K. Ranjana Devi, L. Chaoba Singh, A. Bhargava, U. Gaikwad, G. Vaghela, T. Sukharamwala, A. Ch. Phukan, C. Lyngdoh, R. Saksena, R. Sharma, A. Velayudhan, *Lancet Glob Health* **2022**, *10*, e1317, DOI: 10.1016/S2214-109X(22)00274-1.

[12] M. V. Murhekar, C. G. Kumar, *Lancet Glob Health* **2022**, *10*, e1222, DOI: 10.1016/S2214-109X(22)00317-5.

[13] A. Mehta, V. D. Rosenthal, Y. Mehta, M. Chakravarthy, S. K. Todi, N. Sen, S. Sahu, R. Gopinath, C. Rodrigues, P. Kapoor, V. Jawali, P. Chakraborty, J. P. Raj, D. Bindhani, N. Ravindra, A. Hegde, M. Pawar, N. Venkatachalam, S. Chatterjee, N. Trehan, T. Singhal, N. Damani, *Journal of Hospital Infection* **2007**, *67*, 168, DOI: 10.1016/j.jhin.2007.07.008.

[14] R. Lohiya, V. Deotale, *GMS Hyg Infect Control* **2023**, *18*, Doc28, DOI: 10.3205/DGKH000454.

[15] Y. Karuppiah, *Apollo Medicine* **2024**, DOI: 10.1177/09760016241262582.

[16] M. A. Rather, K. Gupta, P. Bardhan, M. Borah, A. Sarkar, K. S. H. Eldiehy, S. Bhuyan, M. Mandal, *J Basic Microbiol* **2021**, *61*, 380, DOI: 10.1002/JOBM.202000678.

[17] N. Bouhrour, P. H. Nibbering, F. Bendali, *Pathogens* **2024**, *13*, 393, DOI: 10.3390/PATHOGENS13050393.

[18] A. Mishra, A. Aggarwal, F. Khan, *Antibiotics* **2024**, *13*, 623, DOI: 10.3390/ANTIBIOTICS13070623.

[19] M. K. Pal, M. Lavanya, *J Bio Tribocorros* **2022**, *8*, 1, DOI: 10.1007/S40735-022-00677-X.

[20] E. Zhang, X. Zhao, J. Hu, R. Wang, S. Fu, G. Qin, *Bioact Mater* **2021**, *6*, 2569, DOI: 10.1016/J.BIOACTMAT.2021.01.030.

[21] S. Kumar, D. N. Roy, V. Dey, *Colloid Interface Sci Commun* **2021**, *43*, 100464, DOI: 10.1016/J.COLCOM.2021.100464.

[22] M. M. Tunney, S. P. Gorman, S. Patrick, *Drugs* **2012**, *65*, 179, DOI: 10.2165/00003495-200565020-00003.

[23] A. D. S, S. P. A. P, J. Naveen, T. Khan, S. H. Khahro, *Front Bioeng Biotechnol* **2024**, *12*, 1400918, DOI: 10.3389/FBIOE.2024.1400918.

[24] L. Liu, X. Wu, Q. Wang, Z. Yan, X. Wen, J. Tang, X. Li, *Corrosion Reviews* **2022**, *40*, 103, DOI: 10.1515/CORRREV-2021-0039.

[25] J. Knisz, R. Eckert, L. M. Gieg, A. Koerdt, J. S. Lee, E. R. Silva, T. L. Skovhus, B. A. An Stepec, S. A. Wade, *FEMS Microbiol Rev* **2023**, *47*, 1, DOI: 10.1093/FEMSRE/FUAD041.

[26] N. Eliaz, *Materials* **2019**, *12*, 407, DOI: 10.3390/MA12030407.

[27] S. Pandit, K. Gaska, R. Kádár, I. Mijakovic, *ChemPhysChem* **2021**, *22*, 250, DOI: 10.1002/CPHC.202000769.

[28] K. K. A. Mosas, A. R. Chandrasekar, A. Dasan, A. Pakseresht, D. Galusek, *Gels* **2022**, *8*, 323, DOI: 10.3390/GELS8050323.

[29] National Agency for Food & Drug Administration & Control, Drug Evaluation & Research (DER) Directorate, 'NAFDAC GOOD MANUFACTURING PRACTICE FOR MEDICAL DEVICES, IVDs, AND RELATED PRODUCTS GUIDELINES', **2024**.

[30] Aluminium Alloy - Commercial Alloy - 1050A H14 Sheet, *https://www.aalco.co.uk/datasheets/Aluminium-Alloy-1050A-H14-Sheet_57.ashx*, accessed May 5, **2025**.

[31] Y. Y. Avcu, B. Gönül, O. Yetik, F. Sönmez, A. Cengiz, M. Guney, E. Avcu, *Materials* **2021**, *14*, 6575, DOI: 10.3390/MA14216575.

[32] M. Witkowska, G. E. Thompson, T. Hashimoto, E. Koroleva, *Surface and Interface Analysis* **2013**, *45*, 1585, DOI: 10.1002/SIA.5271.

[33] Aluminium: Corrosion, *https://www.alumeco.com/aluminium/corrosion-of-aluminium/?s=0*, accessed May 5, **2025**.

[34] J. S. de Andrade, M. R. S. Vieira, S. H. Oliveira, S. K. de Melo Santos, S. L. Urtiga Filho, *Mater Chem Phys* **2020**, *241*, 122296, DOI: 10.1016/J.MATCHEMPHYS.2019.122296.

[35] J. Sahoo, S. Sarkhel, N. Mukherjee, A. Jaiswal, *ACS Omega* **2022**, *7*, 45962, DOI: 10.1021/ACSOMEGA.2C06211.

[36] S. S. Nasker, P. M. Ajayan, S. Nayak, *ACS Mater Lett* **2023**, *5*, 673, DOI: 10.1021/ACSMATERIALSLETT.2C01116.

[37] M. A. Islam, A. Hossain, N. Hossain, M. M. S. Ahmed, S. Islam, A. M. A. Henaish, A. V. Soldatov, M. A. Chowdhury, *Sensors International* **2024**, *5*, 100293, DOI: 10.1016/J.SINTL.2024.100293.

[38] R. Podila, T. Moore, F. Alexis, A. Rao, *J Vis Exp* **2013**, e50276, DOI: 10.3791/50276.

[39] A. D. Staneva, D. K. Dimitrov, D. N. Gospodinova, T. G. Vladkova, *Microorganisms 2021, Vol. 9, Page 1839* **2021**, *9*, 1839, DOI: 10.3390/MICROORGANISMS9091839.

[40] S. Bhatt, R. Pathak, V. D. Punetha, M. Punetha, *J Mater Sci* **2023**, *58*, 7839, DOI: 10.1007/S10853-023-08534-Z.

[41] B. Polai, A. Samal, S. Ratha, D. Das, S. Kumar Nayak, *Nano Express* **2025**, *6*, 015024, DOI: 10.1088/2632-959X/ADC31E.

[42] H. Huang, H. Guo, J. Qu, al -, Y. Cho, H. Lee, Y. Jeong, Z. Duan, in 'IOP Conference Series: Materials Science and Engineering', *Vol. 493*, IOP Publishing, **2019**, p. 012020, DOI: 10.1088/1757-899X/493/1/012020.

[43] J. Liu, Y. Wu, F. Yan, Y. Yan, F. Wang, G. Zhang, L. Zeng, Y. Ma, J. Guo, Y. Li, P. Zhang, *Prog Org Coat* **2025**, *200*, 108966, DOI: 10.1016/J.PORGCOAT.2024.108966.

[44] D. K. Ojha, B. Polai, S. S. Nasker, A. Mehra, S. R. Das, S. K. Nayak, P. M. Ajayan, S. Nayak, *Adv Mater Interfaces* **2025**, *12*, 2400637, DOI: 10.1002/ADMI.202400637.

[45] X. Wu, L. Lian, S. Yang, G. He, *J Mater Chem C Mater* **2016**, *4*, 8528, DOI: 10.1039/C6TC02424F.

[46] S. Bittolo Bon, L. Valentini, J. M. Kenny, *Chem Phys Lett* **2010**, *494*, 264, DOI: 10.1016/J.CPLETT.2010.06.024.

[47] S. H. Ko, S. W. Kim, S. H. Lee, Y. J. Lee, *Sci Rep* **2023**, *13*, 1, DOI: 10.1038/s41598-023-47693-6.

[48] B. P. Singh, B. K. Jena, S. Bhattacharjee, L. Besra, *Surf Coat Technol* **2013**, *232*, 475, DOI: 10.1016/J.SURFCOAT.2013.06.004.

[49] ASTM G1-03, Standard Practice for Preparing, Cleaning, and Evaluating Corrosion Test Specimens, ASTM International, *https://store.astm.org/g0001-03r17e01.html*, accessed May 5, **2025**.

[50] S. Panda, T. K. Rout, A. D. Prusty, P. M. Ajayan, S. Nayak, *Advanced Materials* **2018**, *30*, 1702149, DOI: 10.1002/ADMA.201702149.

[51] J. Kim, W. H. Khoh, B. H. Wee, J. D. Hong, *RSC Adv* **2015**, *5*, 9904, DOI: 10.1039/C4RA12980F.

[52] J. Horkstra, L. J. Van Der Pauw, N. V. Philips, *Journal of Electronics and Control* **1959**, *7*, 169, DOI: 10.1080/00207215908937197.

[53] I. Y. Konyashin, T. V. Chukalovskaya, *Surf Coat Technol* **1997**, *88*, 5, DOI: 10.1016/S0257-8972(95)02758-0.

[54] F. C. Walsh, C. Ponce de León, C. Kerr, S. Court, B. D. Barker, *Surf Coat Technol* **2008**, *202*, 5092, DOI: 10.1016/J.SURFCOAT.2008.05.008.

[55] S. H. Ahn, J. H. Lee, H. G. Kim, J. G. Kim, *Appl Surf Sci* **2004**, *233*, 105, DOI: 10.1016/J.APSUSC.2004.03.213.

[56] J. Creus, H. Mazille, H. Idrissi, *Surf Coat Technol* **2000**, *130*, 224, DOI: 10.1016/S0257-8972(99)00659-3.

[57] M. Leonhard, B. Zatorska, D. Moser, B. Schneider-Stickler, *Biomed Res Int* **2019**, *2019*, 8051270, DOI: 10.1155/2019/8051270.

[58] A. Kumar, P. K. Vemula, P. M. Ajayan, G. John, *Nat Mater* **2008**, *7*, 236, DOI: 10.1038/NMAT2099.

[59] J. R. Pringle, *Methods Enzymol* **1991**, *194*, 732, DOI: 10.1016/0076-6879(91)94055-H.

[60] X. Wang, J. Bing, Q. Zheng, F. Zhang, J. Liu, H. Yue, L. Tao, H. Du, Y. Wang, H. Wang, G. Huang, *Emerg Microbes Infect* **2018**, *7*, DOI: 10.1038/S41426-018-0095-0.

[61] H. Yue, J. Bing, Q. Zheng, Y. Zhang, T. Hu, H. Du, H. Wang, G. Huang, *Emerg Microbes Infect* **2018**, *7*, DOI: 10.1038/S41426-018-0187-X.

[62] S. Sharma, J. Acharya, M. R. Banjara, P. Ghimire, A. Singh, *BMC Res Notes* **2020**, *13*, 1, DOI: 10.1186/S13104-020-4895-7.

[63] P. Fazii, E. Ciancaglini, G. Riario Sforza, *European Journal of Clinical Microbiology and Infectious Diseases* **2002**, *21*, 373, DOI: 10.1007/S10096-002-0731-3.

[64] E. F. Haney, M. J. Trimble, R. E. W. Hancock, *Nature Protocols 2021 16:5* **2021**, *16*, 2615, DOI: 10.1038/s41596-021-00515-3.

[65] M. P. Murphy, H. Bayir, V. Belousov, C. J. Chang, K. J. A. Davies, M. J. Davies, T. P. Dick, T. Finkel, H. J. Forman, Y. Janssen-Heininger, D. Gems, V. E. Kagan, B. Kalyanaraman, N. G. Larsson, G. L. Milne, T. Nyström, H. E. Poulsen, R. Radi, H. Van Remmen, P. T. Schumacker, P. J. Thornalley, S. Toyokuni, C. C. Winterbourn, H. Yin, B. Halliwell, *Nat Metab* **2022**, *4*, 651, DOI: 10.1038/S42255-022-00591-Z.

[66] P. C. Liao, E. J. Yang, L. A. Pon, *STAR Protoc* **2020**, *1*, 100160, DOI: 10.1016/J.XPRO.2020.100160.

[67] NACE Standard RP0775-2005 - Preparation, Installation, Analysis, and Interpretation of Corrosion Coupons in Oilfield Operations, *https://webstore.ansi.org/standards/nace/nacestandardrp07752005?srsltid=AfmBOooEwMuikXp0sU7qJ4f-5ow1Xs9P2pAvyH7yQjONhMQ4syB9C5-y*, accessed May 5, **2025**.

[68] J. Grossenbacher, M. R. Gullo, F. Dalcanale, G. Blugan, J. Kuebler, S. Lecaudé, H. Tevaearai Stahel, J. Brugger, *J Biomed Mater Res A* **2015**, *103*, 3625, DOI: 10.1002/JBM.A.35477.

[69] K. Lim, R. R. Y. Chua, B. Ho, P. A. Tambyah, K. Hadinoto, S. S. J. Leong, *Acta Biomater* **2015**, *15*, 127, DOI: 10.1016/J.ACTBIO.2014.12.015.

[70] B. S. Necula, J. P. T. M. Van Leeuwen, L. E. Fratila-Apachitei, S. A. J. Zaat, I. Apachitei, J. Duszczyk, *Acta Biomater* **2012**, *8*, 4191, DOI: 10.1016/J.ACTBIO.2012.07.005.

[71] G. K. Das, P. P. Y. Chan, A. Teo, J. S. C. Loo, J. M. Anderson, T. T. Y. Tan, *J Biomed Mater Res A* **2010**, *93*, 337, DOI: 10.1002/JBM.A.32533.

[72] X. Liu, K. Shan, X. Shao, X. Shi, Y. He, Z. Liu, J. A. Jacob, L. Deng, *Int J Nanomedicine* **2021**, *16*, 753, DOI: 10.2147/IJN.S289008.

[73] ISO 10993-5:2009 - Biological evaluation of medical devices — Part 5: Tests for in vitro cytotoxicity, *https://www.iso.org/standard/36406.html*, accessed May 5, **2025**.

[74] L. Liu, D. Mandler, *Electrochem commun* **2020**, *120*, 106830, DOI: 10.1016/J.ELECOM.2020.106830.

[75] J. Bin Wu, M. L. Lin, X. Cong, H. N. Liu, P. H. Tan, *Chem Soc Rev* **2018**, *47*, 1822, DOI: 10.1039/C6CS00915H.

[76] S.-G. Kim, O.-K. Park, J. H. Lee, B.-C. Ku, *Carbon letters* **2013**, *14*, 247, DOI: 10.5714/CL.2013.14.4.247.

[77] M. Kong, M. Garriga, J. S. Reparaz, M. I. Alonso, *ACS Omega* **2022**, *7*, 39429, DOI: 10.1021/ACSOMEGA.2C05945.

[78] S. H. Chang, C. H. Chiang, F. S. Kao, C. L. Tien, C. G. Wu, *IEEE Photonics J* **2014**, *6*, DOI: 10.1109/JPHOT.2014.2331254.

[79] Y. Raghupathy, A. Kamboj, M. Y. Rekha, N. P. Narasimha Rao, C. Srivastava, *Thin Solid Films* **2017**, *636*, 107, DOI: 10.1016/J.TSF.2017.05.042.

[80] X. He, W. Zhou, *Sci Rep* **2024**, *14*, 1, DOI: 10.1038/S41598-024-71736-1;SUBJMETA=301,638,639,925;KWRD=CHEMISTRY,MATERIALS+SCIENCE,NANOSCIENCE+AND+TECHNOLOGY.

[81] S. Amiri, *Silicon* **2025**, 1, DOI: 10.1007/S12633-025-03298-4.

[82] M. Lipińska, P. Bazarnik, M. Lewandowska, *Archives of Civil and Mechanical Engineering* **2016**, *16*, 717, DOI: 10.1016/j.acme.2016.04.013.

[83] R. Zhou, J. D. Embury, J. T. Wood, J. L. Smith, *Mater Charact* **1996**, *37*, 239, DOI: 10.1016/S1044-5803(96)00179-9.

[84] S. Raygan, H. E. Mofrad, M. Pourabdoli, F. K. Ahadi, *J Mater Process Technol* **2011**, *211*, 1810, DOI: 10.1016/J.JMATPROTEC.2011.06.002.

[85] D. B. Hani, R. Al Athamneh, Z. Albataineh, M. Rawashdeh, I. Makableh, *Crystals (Basel)* **2022**, *12*, 457, DOI: 10.3390/CRYST12040457.

[86] C. H. Lin, W. T. Yeh, C. H. Chan, C. C. Lin, *Nanoscale Res Lett* **2012**, *7*, 1, DOI: 10.1186/1556-276X-7-343.

[87] S. J. An, Y. Zhu, S. H. Lee, M. D. Stoller, T. Emilsson, S. Park, A. Velamakanni, J. An, R. S. Ruoff, *Journal of Physical Chemistry Letters* **2010**, *1*, 1259, DOI: 10.1021/JZ100080C.

[88] N. Yadav, A. Dubey, S. Shukla, C. P. Saini, G. Gupta, R. Priyadarshini, B. Lochab, *ACS Omega* **2017**, *2*, 3070, DOI: 10.1021/ACSOMEGA.7B00371.

[89] X. Zou, L. Zhang, Z. Wang, Y. Luo, *J Am Chem Soc* **2016**, *138*, 2064, DOI: 10.1021/JACS.5B11411.

[90] S. I. Saeed, L. Vivian, C. W. S. C. W. Zalati, N. I. M. Sani, E. Aklilu, M. Mohamad, A. A. M. Noor, K. Muthoosamy, N. F. Kamaruzzaman, *BMC Vet Res* **2023**, *19*, 1, DOI: 10.1186/S12917-022-03560-6.

[91] S. Sharma, J. Mohler, S. D. Mahajan, S. A. Schwartz, L. Bruggemann, R. Aalinkeel, *Microorganisms* **2023**, *11*, 1614, DOI: 10.3390/MICROORGANISMS11061614.

[92] Y. Zhou, H. Wang, C. Zhang, Q. Zhou, D. F. Rodrigues, *Front Mater* **2022**, *9*, 910152, DOI: 10.3389/FMATS.2022.910152.

[93] G. Cao, J. Yan, X. Ning, Q. Zhang, Q. Wu, L. Bi, Y. Zhang, Y. Han, J. Guo, *Colloids Surf B Biointerfaces* **2021**, *200*, 111588, DOI: 10.1016/J.COLSURFB.2021.111588.

[94] P. Zhang, Z. Guo, C. Chen, I. Lynch, *Nano Today* **2022**, *43*, 101436, DOI: 10.1016/J.NANTOD.2022.101436.

[95] C. Martini, F. Longo, R. Castagnola, L. Marigo, N. M. Grande, M. Cordaro, M. Cacaci, M. Papi, V. Palmieri, F. Bugli, M. Sanguinetti, *Antibiotics* **2020**, *9*, 692, DOI: 10.3390/ANTIBIOTICS9100692.

[96] A. Krasowska, K. Sigler, *Front Cell Infect Microbiol* **2014**, *4*, 102373, DOI: 10.3389/FCIMB.2014.00112.

[97] A. Kessler, J. Hedberg, E. Blomberg, I. Odnevall, *Nanomaterials* **2022**, *12*, 1922, DOI: 10.3390/NANO12111922.

[98] J. J. Morris, A. L. Rose, Z. Lu, *Redox Biol* **2022**, *52*, 102285, DOI: 10.1016/J.REDOX.2022.102285.

[99] A. Wojtala, M. Bonora, D. Malinska, P. Pinton, J. Duszynski, M. R. Wieckowski, *Methods Enzymol* **2014**, *542*, 243, DOI: 10.1016/B978-0-12-416618-9.00013-3.

[100] G. E. Villalpando-Rodriguez, S. B. Gibson, *Oxid Med Cell Longev* **2021**, *2021*, 9912436, DOI: 10.1155/2021/9912436.

[101] M. Yousefi, M. Dadashpour, M. Hejazi, M. Hasanzadeh, B. Behnam, M. de la Guardia, N. Shadjou, A. Mokhtarzadeh, *Materials Science and Engineering: C* **2017**, *74*, 568, DOI: 10.1016/J.MSEC.2016.12.125.

[102] G. Pizzino, N. Irrera, M. Cucinotta, G. Pallio, F. Mannino, V. Arcoraci, F. Squadrito, D. Altavilla, A. Bitto, *Oxid Med Cell Longev* **2017**, *2017*, 8416763, DOI: 10.1155/2017/8416763.

[103] S. K. Pramanik, M. Bhuiyan, D. Robert, R. Roychand, L. Gao, I. Cole, B. K. Pramanik, *Science of The Total Environment* **2024**, *921*, 171231, DOI: 10.1016/J.SCITOTENV.2024.171231.

[104] S. A. Park, J. G. Kim, Y. S. He, K. S. Shin, J. B. Yoon, *Physics of Metals and Metallography* **2014**, *115*, 1285, DOI: 10.1134/S0031918X14130201.

[105] Y. Li, D. Xu, C. Chen, X. Li, R. Jia, D. Zhang, W. Sand, F. Wang, T. Gu, *J Mater Sci Technol* **2018**, *34*, 1713, DOI: 10.1016/J.JMST.2018.02.023.

[106] C. Ejileugha, K. M. Ezealisiji, A. N. Ezejiofor, O. E. Orisakwe, *J Bio Tribocorros* **2021**, *7*, 1, DOI: 10.1007/S40735-021-00545-0.

[107] R. Zuo, *Appl Microbiol Biotechnol* **2007**, *76*, 1245, DOI: 10.1007/S00253-007-1130-6.

[108] I. Khosravi, Z. Shahryari, S. M. Jazaeri Moghadas, M. Yeganeh, H. T. Sarraf, *Corrosion Protection at the Nanoscale* **2020**, 127, DOI: 10.1016/B978-0-12-819359-4.00008-8.

[109] Y. Guo, Z. Xu, Q. Wang, S. Zu, M. Liu, Z. Yu, Z. Zhang, L. Ren, *Prog Org Coat* **2022**, *164*, 106722, DOI: 10.1016/J.PORGCOAT.2022.106722.

[110] M. I. Necolau, A. M. Pandele, *Coatings* **2020**, *10*, 1149, DOI: 10.3390/COATINGS10121149.

[111] S. J. Richard Prabakar, Y. H. Hwang, E. G. Bae, D. K. Lee, M. Pyo, *Carbon N Y* **2013**, *52*, 128, DOI: 10.1016/J.CARBON.2012.09.013.

[112] T. Mosmann, *J Immunol Methods* **1983**, *65*, 55, DOI: 10.1016/0022-1759(83)90303-4.

[113] I. Koyuncu, A. Gönel, A. Akdağ, M. A. Yilmaz, *Cell Mol Biol* **2018**, *64*, 75, DOI: 10.14715/CMB/2018.64.1.14.

[114] S. Gurunathan, M. A. Iqbal, M. Qasim, C. H. Park, H. Yoo, J. H. Hwang, S. J. Uhm, H. Song, C. Park, J. T. Do, Y. Choi, J. H. Kim, K. Hong, *Nanomaterials* **2019**, *9*, 969, DOI: 10.3390/NANO9070969.

[115] M. R. Rahimzadeh, M. R. Rahimzadeh, S. Kazemi, R. J. Amiri, M. Pirzadeh, A. A. Moghadamnia, *Emerg Med Int* **2022**, *2022*, 1480553, DOI: 10.1155/2022/1480553.

[116] C. Exley, *Environ Sci Process Impacts* **2013**, *15*, 1807, DOI: 10.1039/C3EM00374D.

[117] K. Catt, H. Li, X. T. Cui, *Acta Biomater* **2017**, *48*, 530, DOI: 10.1016/J.ACTBIO.2016.11.039.

[118] V. Srimaneepong, D. Rokaya, P. Thunyakitpisal, J. Qin, K. Saengkiettiyut, *Sci Rep* **2020**, *10*, 1, DOI: 10.1038/s41598-020-60070-x.

[119] S. P. Cangui-Panchi, A. L. Ñacato-Toapanta, L. J. Enríquez-Martínez, J. Reyes, D. Garzon-Chavez, A. Machado, *Curr Res Microb Sci* **2022**, *3*, 100175, DOI: 10.1016/J.CRMICR.2022.100175.

[120] L. Carpen, P. Rajala, M. Bomberg, *Corrosion Science and Technology* **2018**, *17*, 147, DOI: 10.14773/CST.2018.17.4.147.

[121] S. J. Salgar-Chaparro, K. Lepkova, T. Pojtanabuntoeng, A. Darwin, L. L. Machuca, *Corros Sci* **2020**, *169*, 108595, DOI: 10.1016/J.CORSCI.2020.108595.

[122] D. Xu, Y. Li, T. Gu, *Bioelectrochemistry* **2016**, *110*, 52, DOI: 10.1016/J.BIOELECHEM.2016.03.003.

[123] E. Puentes-Cala, V. Tapia-Perdomo, D. Espinosa-Valbuena, M. Reyes-Reyes, D. Quintero-Santander, S. Vasquez-Dallos, H. Salazar, P. Santamaría-Galvis, R. Silva-Rodríguez, G. Castillo-Villamizar, *Front Environ Sci* **2022**, *10*, 924842, DOI: 10.3389/FENVS.2022.924842.

[124] Brinda, M. S. Divyashree, S. A. Rao, P. Rao, L. Mulky, *Journal of Chemical Technology & Biotechnology* **2025**, *100*, 1143, DOI: 10.1002/JCTB.7848.

[125] S. Monaci, D. Minudri, A. J. U. Aird, D. Mantione, D. Mecerreyes, A. Somers, M. Forsyth, *Prog Org Coat* **2025**, *200*, 109000, DOI: 10.1016/J.PORGCOAT.2024.109000.

Enhancing the biocorrosion resistance and biocompatibility of Aluminium substrates using Graphene Oxide-PEDOT:PSS Hybrid Coating

*Sourya Subhra Nasker[1], Ragnhild Elizabeth Aune[2], Amogh K. Ravi[3], Tharangattu N. Narayanan[3], and Sasmita Nayak[1,4]**

[1]School of Biotechnology, Kalinga Institute of Industrial Technology (KIIT), Bhubaneswar, Odisha 751024, India
[2]Department of Materials Science and Engineering, Norwegian University of Science and Technology (NTNU), 7491 Trondheim, Norway
[3]Materials and Interface Engineering Laboratory, Tata Institute of Fundamental Research (TIFR), Hyderabad, Telangana 500046, India
[4]Department of Microbiology, Kalinga Institute of Medical Sciences, Kalinga Institute of Industrial Technology Deemed to be University, Bhubaneswar, Odisha 751024, India

**Address all correspondence to Dr. Sasmita Nayak; E-mail: sasmita.n@kiitbiotech.ac.in*

Table of Contents

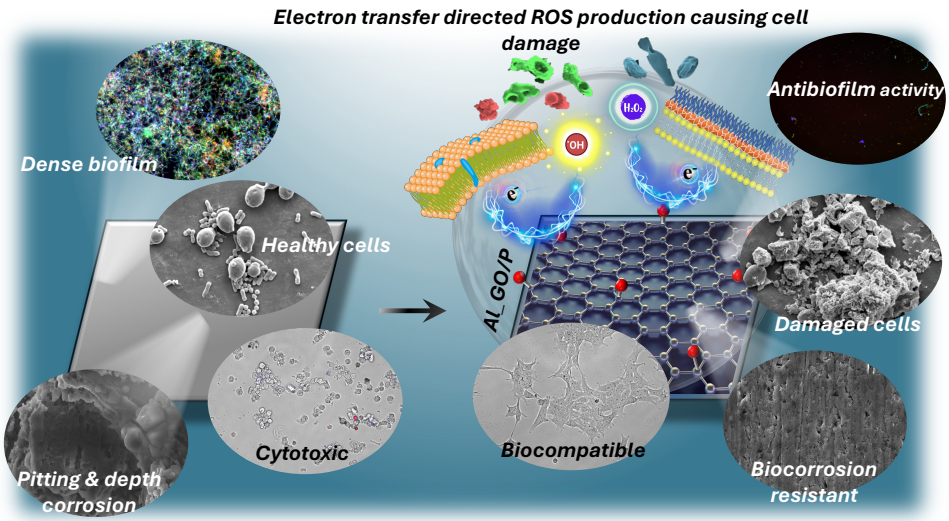

Schematic illustration (*from left to right*) highlighting the contrast between biofouling-prone bare Al surfaces, which facilitate microbial colonization, exhibit poor corrosion resistance, and display inherent cytotoxicity. Whereas Al_GO/P surface(s) demonstrate superior antibiofouling activity. The Al_GO/P hybrid surface leverages synergistic mechanisms, like nanoknife effect of GO, increased surface hydrophobicity, and electron extraction facilitated by the conductivity of underneath substrate to induce oxidative stress in microbial cell membranes. In addition to providing remarkable biocorrosion resistance, the Al_GO/P substrates display excellent biocompatibility, making them highly promising for next-generation biomedical implants and healthcare devices that require both long-term durability and cytocompatibility.